ADA046569

SYSTEMS, SCIENCE AND SOFTWARE

SEISMIC STUDIES FOR IMPROVED YIELD DETERMINATION

T. C. Bache
J. M. Savino
M. Baker
P. L. Coleman

Quarterly Technical Report

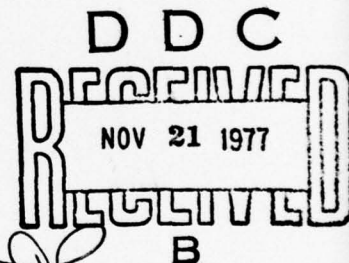For Period October 1 - December 31, 1976

The views and conclusions contained in this document are those of the authors and should not be interpreted as necessarily representing the official policies, either expressed or implied, of the Advanced Research Projects Agency, the Air Force Technical Applications Center, or the U.S. Government.

DDC

NOV 21 1977

B.

January 1977

AD No.

DDC FILE COPY

AFTAC Project Authorization No. VELA/T/7712/B/ETR

Program Code No. 6H189

Effective Date of Contract: October 1, 1976

Contract Expiration Date: September 30, 1977

Amount of Contract: $374,397

Contract No. F08606-76-C-0041

Principal Investigator and Phone No.
  Dr. Thomas C. Bache, (714) 453-0060, Ext. 337

Project Scientist and Phone No.
  Dr. Ralph W. Alewine, III, (202) 325-8484

REPORT DOCUMENTATION PAGE		READ INSTRUCTIONS BEFORE COMPLETING FORM
1. REPORT NUMBER	2. GOVT ACCESSION NO.	3. RECIPIENT'S CATALOG NUMBER
4. TITLE (and Subtitle) SEISMIC STUDIES FOR IMPROVED YIELD DETERMINATION.		5. TYPE OF REPORT & PERIOD COVERED Quarterly 10/1/76-12/31/76
		6. PERFORMING ORG. REPORT NUMBER SSS-R-77-3108
7. AUTHOR(s) T. C. Bache, J. M. Savino, M. Baker and P. Coleman		8. CONTRACT OR GRANT NUMBER(s) F08606-76-C-0041 ARPA Order-2551
9. PERFORMING ORGANIZATION NAME AND ADDRESS Systems, Science and Software P. O. Box 1620 La Jolla, California 92038		10. PROGRAM ELEMENT, PROJECT, TASK AREA & WORK UNIT NUMBERS Program Code 6H189 Project Authorization No. VELA/T/7712/B/ETR
11. CONTROLLING OFFICE NAME AND ADDRESS VELA Seismological Center 312 Montgomery Street Alexandria, VA 22314		12. REPORT DATE January 1977
		13. NUMBER OF PAGES
14. MONITORING AGENCY NAME & ADDRESS(if different from Controlling Office) Quarterly technical rept. 1 Oct - 31 Dec 76,	86p.	15. SECURITY CLASS. (of this report) Unclassified
		15a. DECLASSIFICATION/DOWNGRADING SCHEDULE

16. DISTRIBUTION STATEMENT (of this Report)

no. 1

Approved for Public Release, Distribution Unlimited

17. DISTRIBUTION STATEMENT (of the abstract entered in Block 20, if different from Report)

18. SUPPLEMENTARY NOTES

(M sub s and m s

19. KEY WORDS (Continue on reverse side if necessary and identify by block number)

Explosion Source Modeling, Yield Determination, Cratering Explosions, Seismic Attenuation, Theoretical Seismogram Generation

The main objective of this contract

20. ABSTRACT (Continue on reverse side if necessary and identify by block number)

The report summarizes the results of the first three months of research on a contract whose main objective is to examine the parameters that affect the seismic signals from underground explosions. Results are presented from research in five areas: (1) Theoretical teleseismic magnitudes (M_s and m_b) were determined for a series of nuclear explosion cratering calculations carried out by Applied Theory, Inc. (2) The relative frequency content of signals from U.S.S.R. and U.S. explosions were studied by comparing the periods of the first few cycles of recordings from several stations at teleseismic ranges; (3) Some improved

(conton p1473B)

388 507

(cont &p)
(1473A)

20. techniques were developed for computing the equivalent point source representation for explosions in highly porous materials; (4) The dependence of body wave magnitude on yield for underground explosions in salt was studied and compared to that for explosions in granite; and (5) Small scale experiments were carried out in which underground explosions were modeled by 0.25 gram charges embedded in concrete.

1473B

TABLE OF CONTENTS

I. SUMMARY

The objective of our research program is to examine the parameters that affect the seismic signals from underground explosions. Our attention is primarily directed to those features of the seismic waveforms that reliably indicate the explosion yield. Our research program includes empirical studies of the available data, experimental studies using small charges to simulate explosions and the development and application of theoretical and numerical methods. Emphasis is on the latter, in particular we are applying techniques for numerically simulating the far-field signals from both contained and cratering underground explosions. The numerical simulation techniques represent a synthesis of the finite difference methods for computing ground motion in the near-source large displacement regime and the efficient wave propagation techniques of theoretical seismology.

During the first three-month period of our present contract, our research activities have been concentrated in five areas. These areas and the major results obtained in each are summarized in the next five paragraphs.

We have been involved in a joint project with Applied Theory, Inc. (ATI) and Pacific Sierra Research (PSR) in which the main objective has been to study the variation of the teleseismic magnitudes, M_s and m_b, with source material and depth for a series of cratering calculations. Our contribution has been to process the output of the ATI calculations and obtain estimates of M_s and m_b. A detailed report is being prepared describing our techniques and results. In Section 3.1 of this report we present the synthetic seismograms and the m_b and M_s values we have computed. These results are presented without comment regarding their significance or importance for treaty monitoring. Such comments will be more appropriate after detailed consultation with ATI and PSR scientists and will appear in our topical report.

An important question now under study at many institutions is the possibility that NTS may be underlain by a region of anomalously high attenuation which causes the m_b from NTS explosions to be biased low. We have also been studying this question. As a first step we have compared the frequency content of a large population of NTS and Eurasian explosions at several recording stations where we have previous experience in synthesizing short period recordings of NTS events. Our results are shown graphically and discussed in Section 3.2. We conclude that the dominant periods for Kazakhstan events are considerably shorter than for NTS events in the same yield range. The differences are as much as 0.5 seconds at two of the stations. A significant point about the NTS data is that the period of the PILEDRIVER event, an unusual NTS explosion in granite, falls within the NTS population. While these data do not argue conclusively for differences in attenuation being the cause of the observed frequency differences, they point in that direction, particularly in view of the large sampling of event depths and source media. We are continuing to study this problem using our synthetic seismogram generating capabilities.

An important part of our research capability is our numerical (finite difference) techniques for simulating the coupling of the explosion energy into elastic waves in the earth. Using our one-dimensional (spherically symmetric) computer code, we have been studying the effect of near source material properties on the seismic signal. Our previously developed constitutive models were found to be unsatisfactory when used for highly porous materials. Our constitutive models were reevaluated and the results are discussed in Section 3.3. A minor modification to the constitutive model was found to enable the program to give excellent results for highly porous materials. The new model is as compatible with laboratory data as was the one previously used.

During the quarter, a theoretical study was conducted
in which the objective was to compare explosions in salt in
Eurasia to similar, though hypothetical, events at NTS and
to granite events at NTS. The results of this study were
presented in detail in a topical report by Bache, Cherry
and Mason [1976]. The main results from that report are
given here in Section 3.4. A series of equivalent point
source representations for explosions at various depths in
salt were computed. We found that the long period level,
proportional to M_s, was only mildly sensitive to depth. The
short period level, however, was much more sensitive, varying
by a factor of two for depths between 150 and 2500 meters.
This is due to the opening of tensile cracks in the material
at the low confining pressures characteristic of shallow
depths. We found that when all other factors are the same,
explosions in salt couple about a factor of two smaller than
events in PILEDRIVER-type granite. We also looked at the
effect of attenuation on the seismograms. If we assume the
attenuation for NTS events is about 40 percent higher than
for Eurasian events, we find that identical salt explosions
at the two test sites would give body wave amplitudes that
differ by a factor of $\approx$ 3-4.

We have been engaged in an experimental program in
which small-scale modeling experiments of underground explo-
sions are to be compared to computer simulations of the
experiments. After some difficulties with the explosives
and displacement gauges which took several months to resolve,
several successful modeling experiments have been carried
out. The test medium is a concrete cylinder and the charges
are 0.25 grams of PETN explosive which can be buried at
selected depths. In Section 3.5 we give some results from
our first experiments. These results indicate the reliability
and repeatability of the experiments and are necessary to
lend credibility to the results. The ground motion records
are of excellent quality and we are now proceeding to

numerically model these experiments. These should provide an excellent normalization of our theoretical techniques. Further experiments are being performed in which the charge will be shallow so cratering will result.

II. INTRODUCTION

The primary objective of the research program is to systematically examine the parameters that control magnitude-yield relationships for underground nuclear explosions. During the first three month period of this contract, activity has been concentrated in the following areas:

1. The calculation of teleseismic magnitudes (M_s and m_b) for nuclear explosion cratering calculations carried out by Applied Theory, Incorporated.

2. The study of body wave attenuation properties for selected non-U.S. travel paths.

3. Development of improved techniques for one-dimensional numerical simulation of explosions.

4. A study of the dependence of body wave magnitude on yield for underground explosions in salt.

5. A laboratory simulation of underground explosions (project carried over from our previous contract, Project VT/6712).

The following section, the Technical Discussion, is devoted to technical summaries of our work in each of the above listed areas.

III. TECHNICAL DISCUSSION

3.1   CALCULATION OF M_s, m_b FOR ATI CRATERING CALCULATIONS

3.1.1 Introduction

We are involved in a joint project with Applied Theory, Incorporated (ATI) and Pacific Sierra Research (PSR) to study the variation of the teleseismic magnitudes, M_s and m_b, with source material and depth for a series of cratering calculations. The S^3 function has been to process the output of the finite difference calculations performed by ATI and to determine M_s and m_b for each calculation. This is a complex and rather difficult task and a detailed report is being prepared describing our techniques and the results. In this report we will present the most important results. We would like to point out that the results are preliminary and some changes may result after consultation with ATI and PSR scientists.

3.1.2 Computational Procedure

Briefly outlined, the computational procedure followed to obtain M_s and m_b for the cratering calculations is as follows:

1.   The ATI performed cratering calculations were carried into the regime where the material response is approximately linearly elastic. A tape was then prepared containing the time histories of the divergence and curl ($\nabla \cdot \underset{\sim}{u}(t)$, $\nabla \times \underset{\sim}{u}(t)$) of the displacement field on a radius, denoted the elastic radius, centered at ground zero. The geometry and coordinate system are shown in Figure 3.1.1.

2.   The divergence and curl are expanded in a series of spherical harmonics to obtain an equivalent elastic source. The procedure is formally that described by
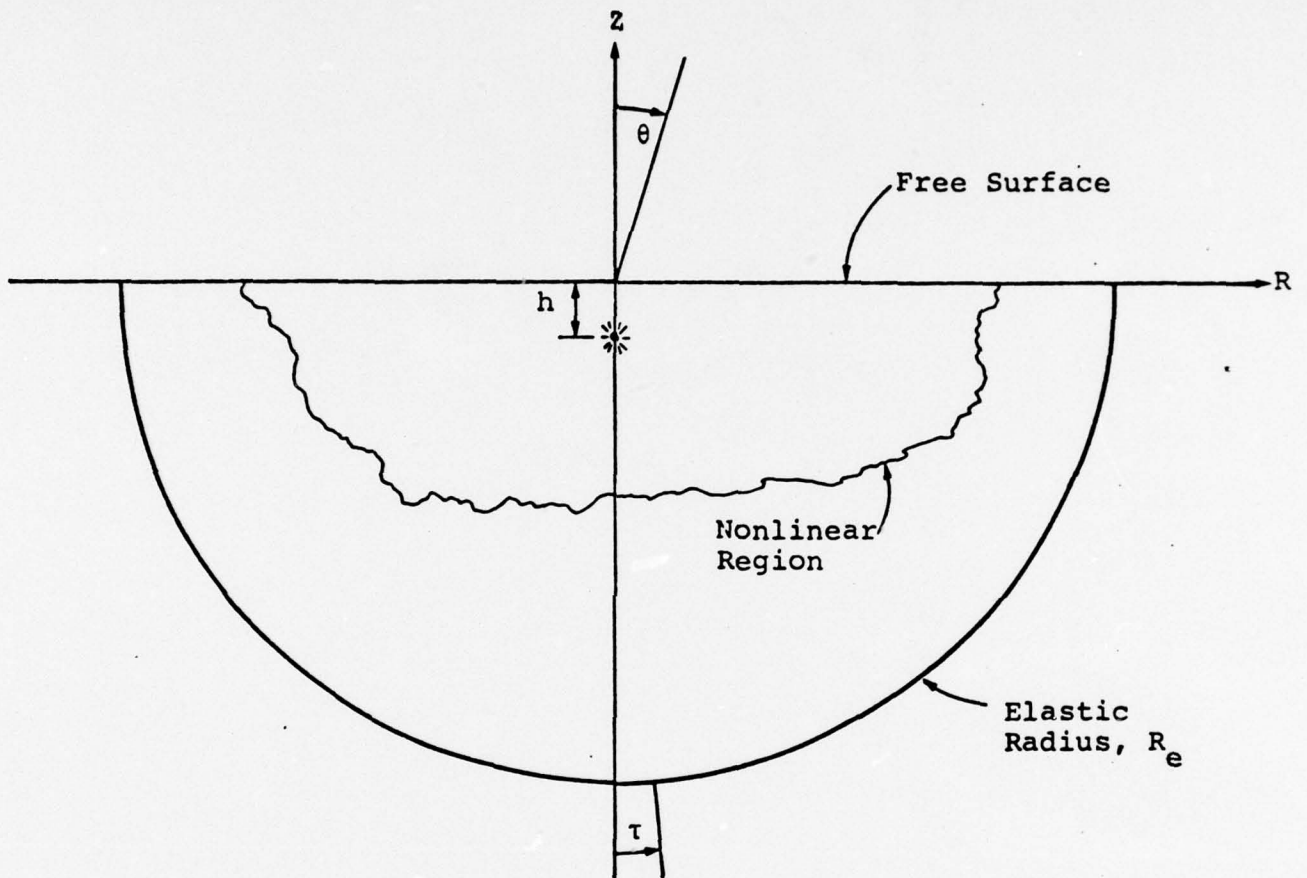
6

Figure 3.1.1. The geometry and coordinate system for the
cratering calculations. The solution is inde-
pendent of the azimuthal coordinate.

7

Bache and Harkrider [1976] for sources in a whole
space. However, the presence of a free surface re-
quires a number of assumptions that, to some extent,
control the solution. The extent of this effect is
discussed in some detail in our forthcoming report.
However, the most important point is that all the
cratering calculations are treated the same way and
the relative values of m_b and M_s should be preserved.

3.   Using the equivalent elastic source, synthetic seis-
mograms are computed for body waves and surface
waves. For body waves the pertinent references are
Bache and Harkrider [1976] and Bache, et al. [1976].
For surface waves we use the method of Harkrider
which has been described in numerous publications;
e.g., Harkrider [1964], with certain modifications
indicated in Section 3.1.6.

4.   The values of m_b and M_s are strongly dependent on
the crust and upper mantle models used in the syn-
thetic seismogram calculations. However, the same
models are used in all calculations and the relative
values should be insensitive to these models.

5.   The free surface stresses due to the ejecta fallback
were also provided to us by ATI. These data were
analyzed to determine the effect on the far-field
body and surface waves.

3.1.3   Description of Cratering Calculations

We will be describing fourteen source calculations in
three emplacement materials. Two of these are one-dimensional
calculations for contained explosions in a homogeneous whole
space and provide benchmark cases for measuring the effect of
the cratering. The other twelve are cratering calculations.
The important parameters characterizing the calculations are
summarized in Table 3.1.1.

TABLE 3.1.1

PARAMETERS DESCRIBING THE ATI CALCULATIONS

Identifier	Material	Depth (km)	α (km/sec)	β (km/sec)	ρ (km/sec)
1	Granite	0.159	4.402	2.54	2.661
2	"	0.207	4.402	2.54	2.661
3	"	0.253	4.406	2.542	2.661
4	Dry Sandstone	0.159	2.822	1.740	2.30
5	"	0.207	2.825	1.743	2.30
6	"	0.253	2.828	1.744	2.30
7	"	0.207	2.836	1.755	2.30
8	Wet Sandstone	0.053	2.620	1.509	2.40
9	"	0.159	2.624	1.592	2.40
10	"	0.207	2.614	1.513	2.40
11	"	0.253	2.618	1.517	2.40
12	"	0.531	2.619	1.519	2.40
13	Granite	Spherically Symmetric	4.239	2.448	2.661
14	Wet Sandstone	Spherically Symmetric	2.619	1.530	2.40

We see from the table that the calculations have the potential to help us understand:

1. The effect of burial depth on the teleseismic signature of cratering explosions.

2. The effect of emplacement material on the signal from cratering explosions.

3. The differences between cratering and contained shots in the same material.

Considering the approximations made in our calculations (exclusive of any difficulties with the finite difference calculations), the above are listed in order of the amount of confidence we place in the results.

3.1.4 Far-field Displacement Spectra

For each of the fourteen sources listed in Table 3.1.1 we compute far-field displacement spectra. For the one-dimensional, spherically symmetric calculations the equivalent elastic source is the reduced displacement potential, $\Psi(t-R/\alpha)$, which is related to the displacement by

$$\hat{u}(R,\omega) = \frac{\hat{\Psi}}{R^2} + \frac{\hat{\dot{\Psi}}}{R\alpha} \; , \qquad (3.1.1)$$

where all quantities are Fourier transformed. Then the far-field displacement spectrum is defined by

$$\hat{u}_{ff}(R,\omega) = \frac{\hat{\dot{\Psi}}}{R\alpha} \; . \qquad (3.1.2)$$

An entirely analogous procedure is followed for the complex equivalent elastic source representations of the cratering calculations. That is, we retain only terms of order R^{-1} in the expansion.

The displacement spectra are presented in Figures 3.1.2 - 3.1.7. The plots are log-log in amplitude versus frequency. Note that the scale on the amplitude axis is in powers of 10 while the actual frequencies are printed on the abscissa.

Two frequencies are singled out on the spectra for the cratering calculations and are denoted A and B. The frequency denoted B is associated with the (approximate) total time of the ground motion data provided by ATI. That is, if the $\nabla \cdot \underset{\sim}{u}(t)$ and $\nabla \times \underset{\sim}{u}(t)$ at a typical station on the elastic radius had their first non-zero value at $t_i = 0.4$ seconds and the final time point was at $t_f = 2.5$ seconds, we say that the frequency B is $1/(t_f-t_i)$ or, for this example, 0.48 Hz. Then B is the lowest frequency that can be associated with the actual computed data.

The meaning of the frequency A is more difficult to explain and the interested reader is referred to our forthcoming detailed report. Beyond the time t_f we assume that the lowest order terms (the dipole) in the expansion of the divergence and curl are zero. The higher order terms are assumed to remain static at the value reached at the last time point. The amplitudes at all frequencies below B are dependent on these assumptions. In order to compute the Fourier transform we extend the time histories out to some t_e using the assumptions mentioned above. Then $A \approx 1/(t_e-t_i)$.

How do we compute values for frequencies below A? We know that the response at low frequencies is dominated by the dipole term in the expansion. Further, we can prove that the dipole term must behave like ω^2 at low frequency for a bounded solution. This corresponds to a flat far-field displacement spectrum at low frequency. Our actual procedure is to extrapolate the amplitude of the dipole term from its value at A by assuming proportionality to ω^2. This is nearly the same
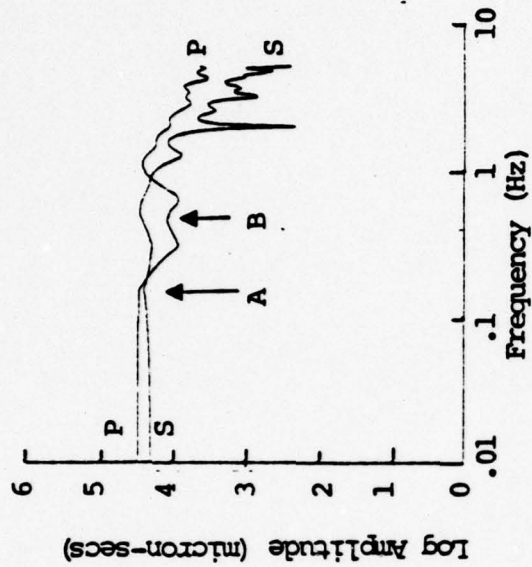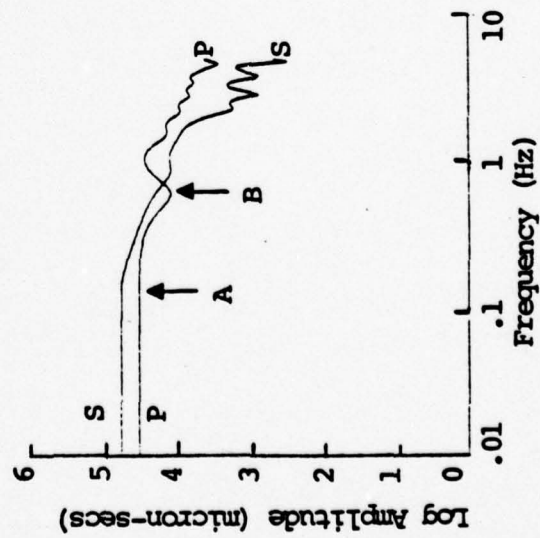
11
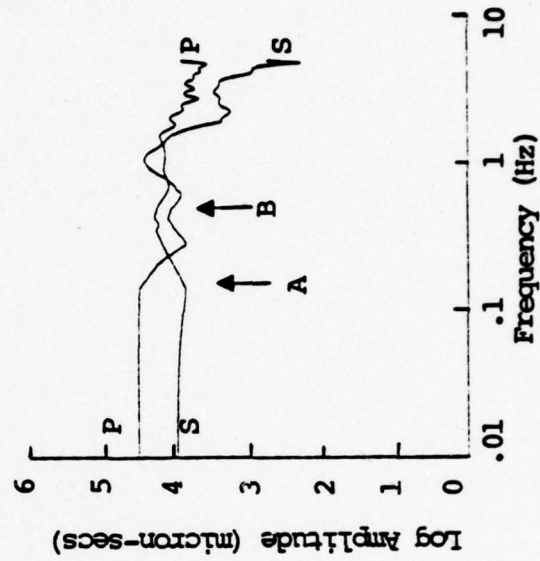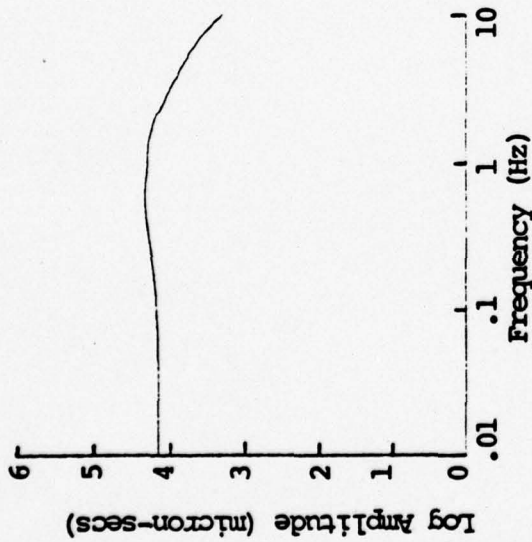
Figure 3.1.2. Far-field displacement spectra for one spherically symmetric and three cratering explosions in granite. The spectra are for a takeoff angle τ = 20°.
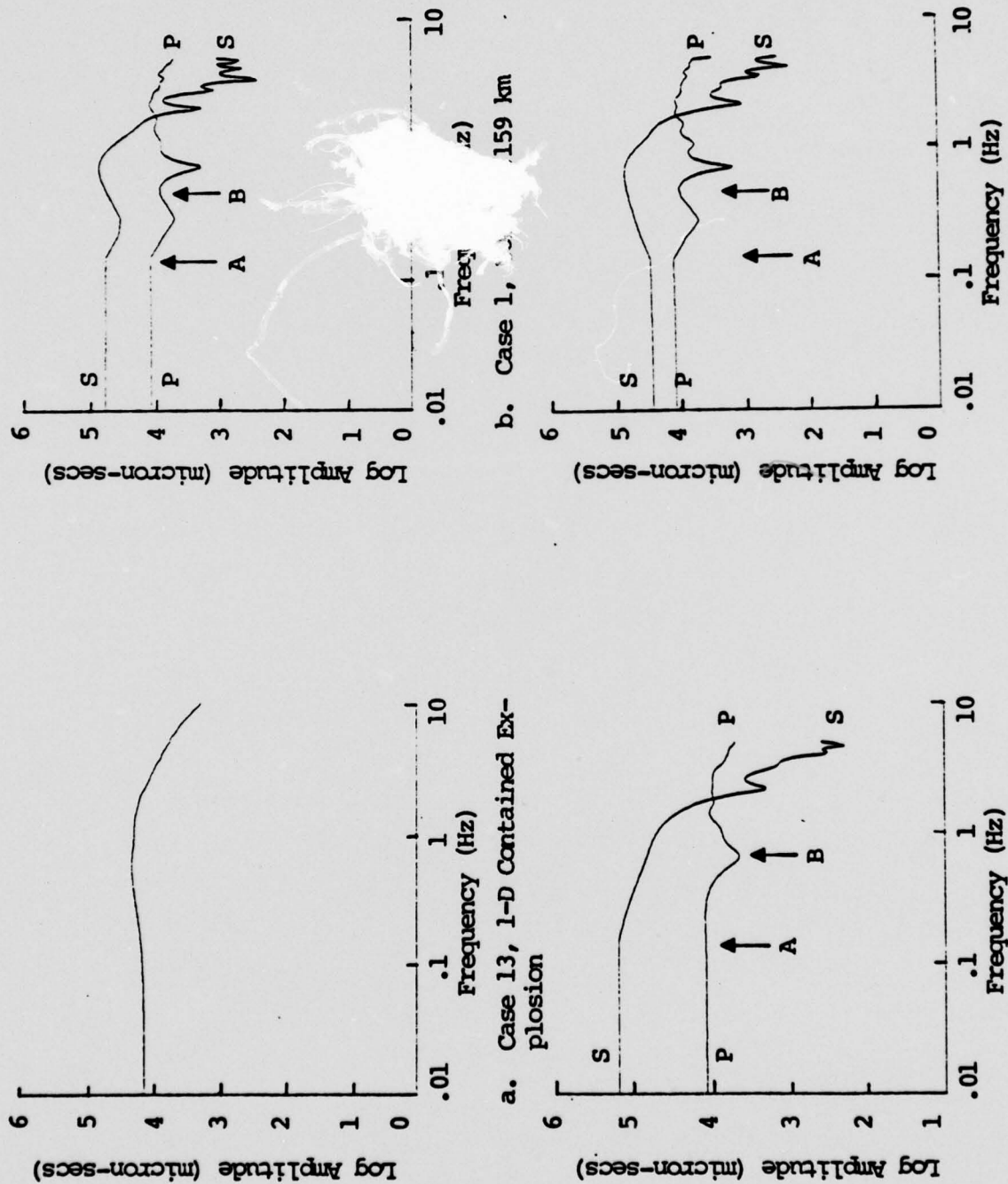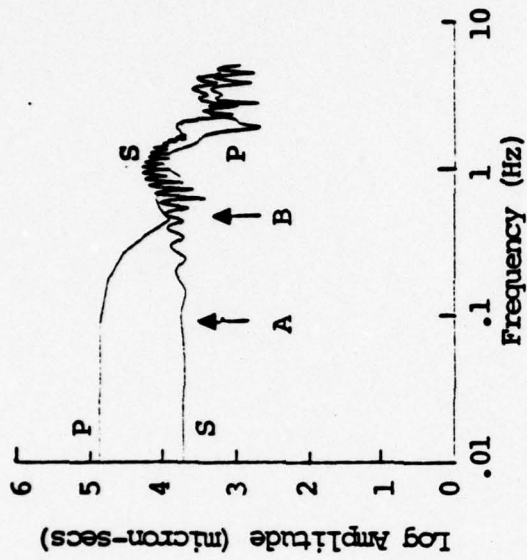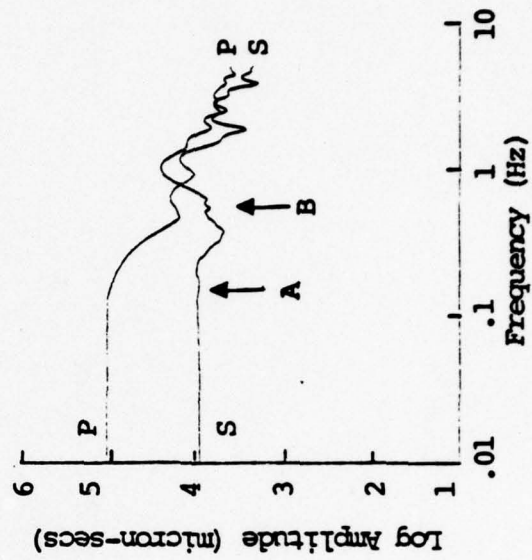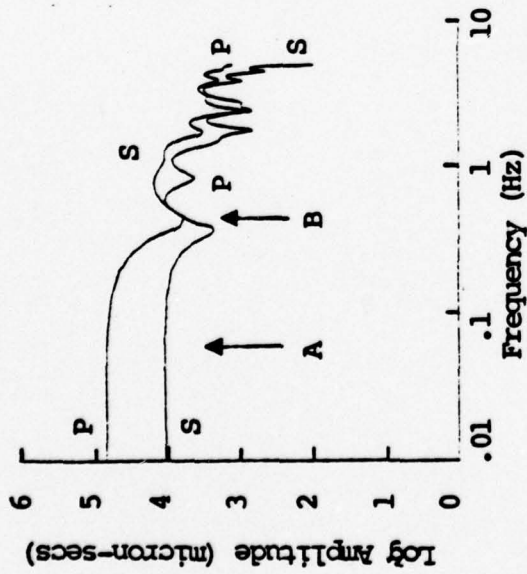
Figure 3.1.3. Far-field displacement spectra for one spherically symmetric and three cratering explosions in granite. The spectra are for a takeoff angle τ = 70°.

Figure 3.1.4. Far-field displacement spectra for four cratering explosions in dry sandstone. The spectra are for a takeoff angle τ = 20°.

14
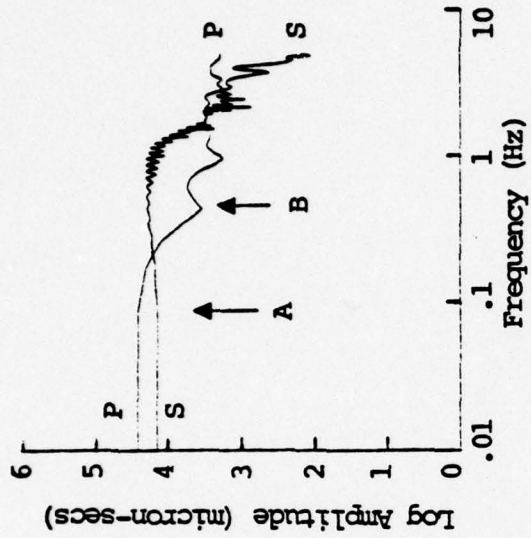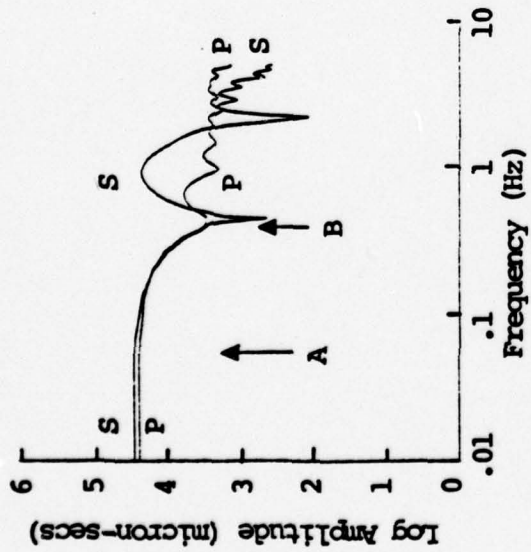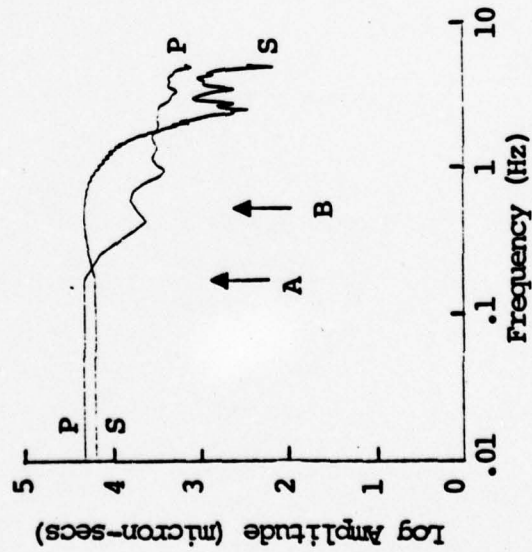
Figure 3.1.5. Far-field displacement spectra for four cratering explosions in dry sandstone. The spectra are for a takeoff angle τ = 70°.
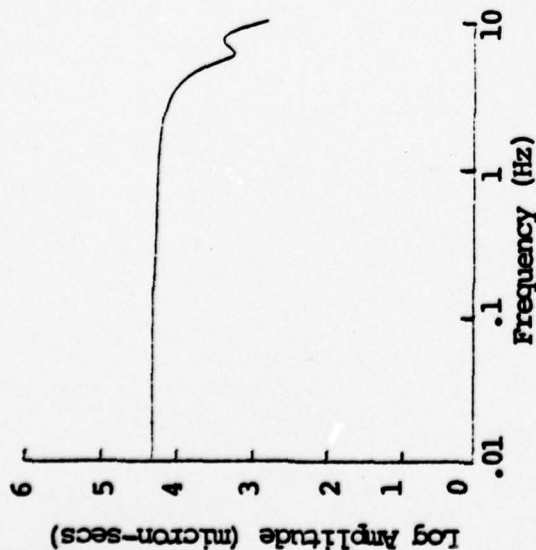
a. Case 14, 1-D Contained Explosion
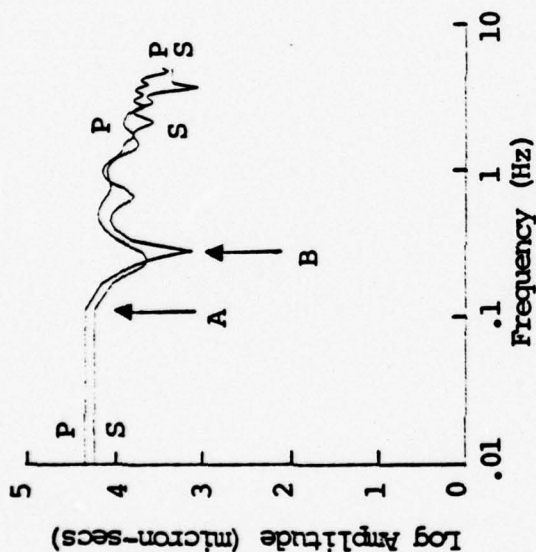
b. Case 8, DOB = 0.053 km
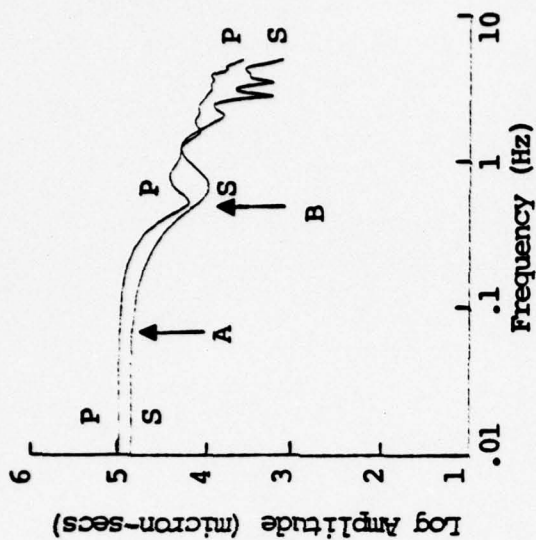
c. Case 9, DOB = 0.159 km

d. Case 10, DOB = 0.207 km

e. Case 11, DOB = 0.253 km

f. Case 12, DOB = 0.531 km

Figure 3.1.6. Far-field displacement spectra for one spherically symmetric and five cratering explosions in wet sandstone. The spectra are for a takeoff angle $\tau = 20°$.
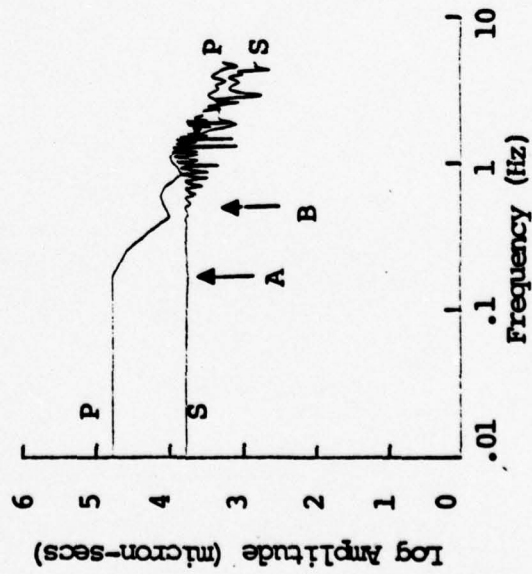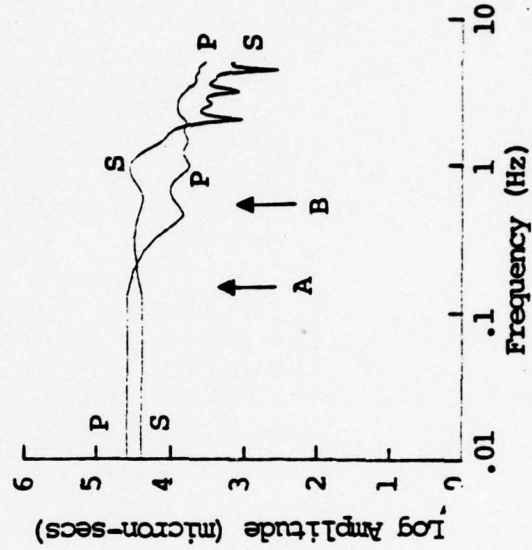
16

a. Case 14, 1-D Contained Explosion

b. Case 8, DOB = 0.053 km
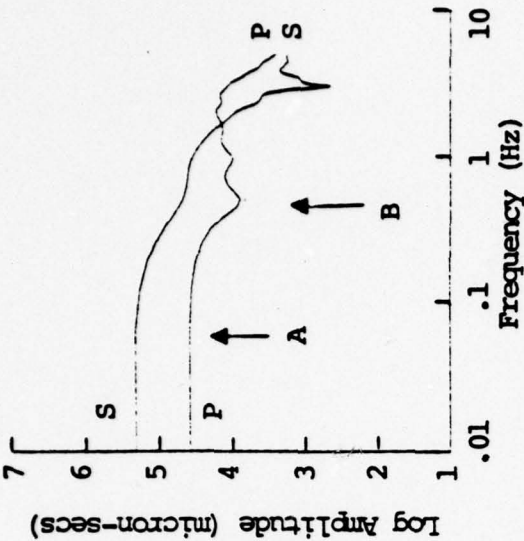
c. Case 9, DOB = 0.159 km
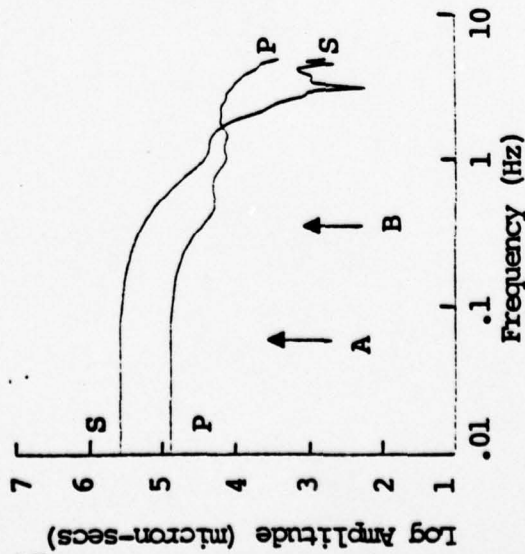
d. Case 10, DOB = 0.207 km
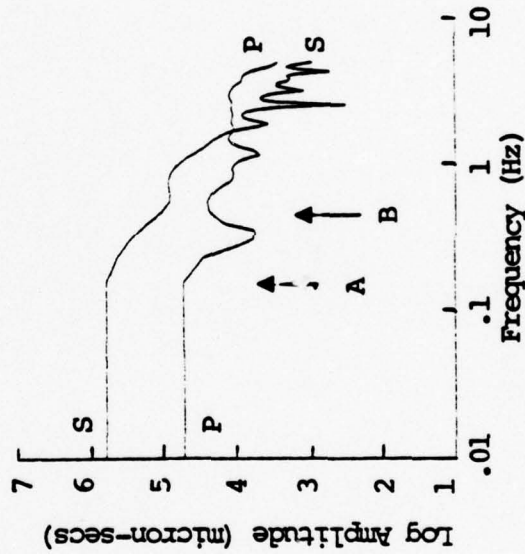
e. Case 11, DOB = 0.253 km
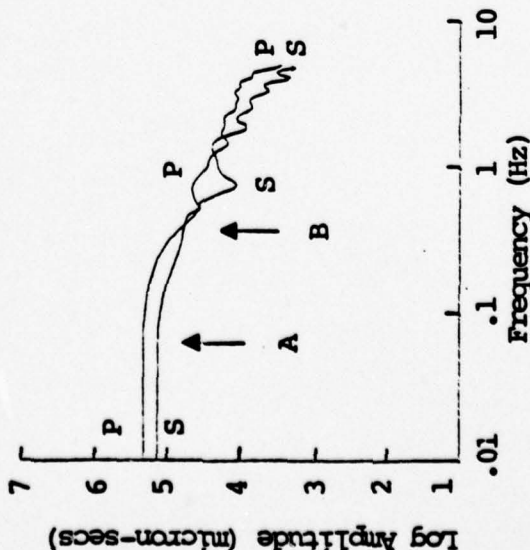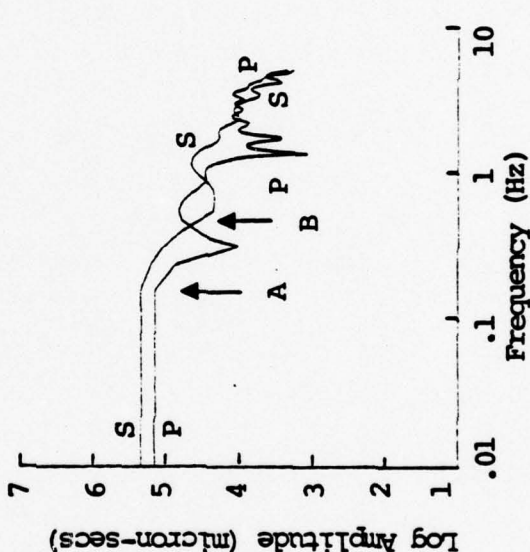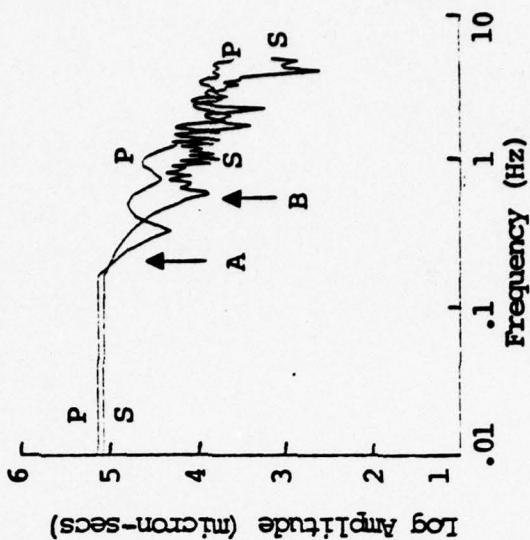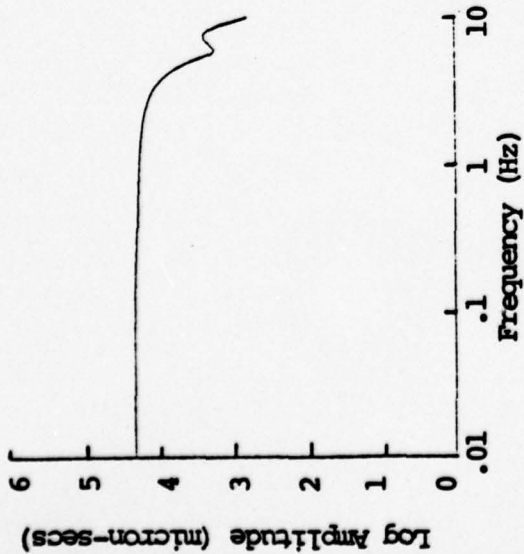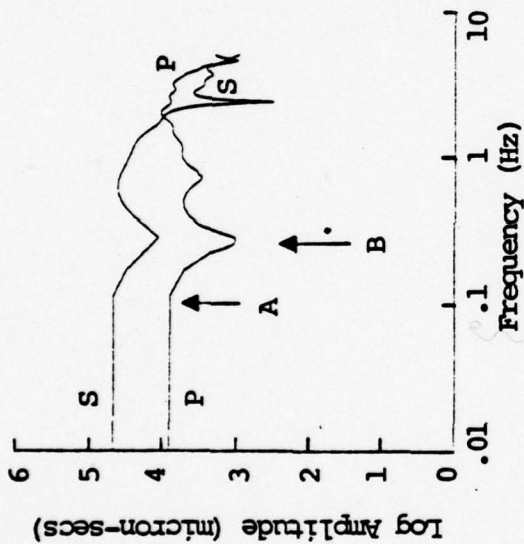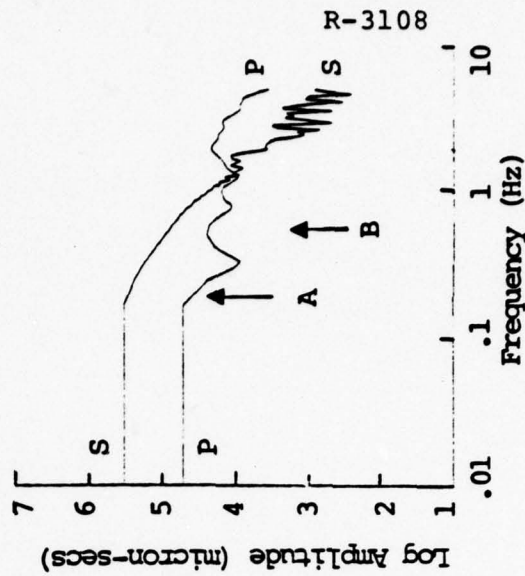
f. Case 12, DOB = 0.531 km

Figure 3.1.7. Far-field displacement spectra for one spherically symmetric and five cratering explosions in wet sandstone. The spectra are for a takeoff angle $\tau = 70°$.

17

as assuming the far-field displacement spectrum to be flat
to long periods from its value at A as can be seen in the
figures.

Finally, in Tables 3.1.2 - 3.1.3 we tabulate the
spectral values that have the greatest significance for com-
puting teleseismic body and surface waves. The amplitude
values in Tables 3.1.2 - 3.1.3 are all on the same scale
(all have been multiplied by 10^{-4} R) and are best viewed as
relative amplitudes. The reliability of these values for
scaling m_b and M_s is discussed in our topical report.

3.1.5 Body Wave Amplitude, m_b

In this section we present our synthetic seismograms
for the fourteen ATI sources and give the m_b values for each.
The synthetic seismogram calculations include the following
elements:

1.   The equivalent elastic sources which give the (whole
      space) far-field displacement spectra described in the
      previous section are embedded in a layered model of
      the crust in the source region. The basic model used
      for the calculations is tabulated in Table 3.1.4.
      The top layer was changed to have the properties ap-
      propriate to each source as listed in Table 3.1.1.
      In carrying out the calculations only the downgoing
      waves emitted by the source are computed; that is,
      no free surface is included in the source crustal
      model.

2.   The far-field body waves emanating from the base of
      the source crust and characterized by ray parameter
      p = 0.079 sec/km are calculated.

3.   The upper mantle is accounted for by a step function
      response computed using generalized ray theory.   In

18

TABLE 3.1.2

BODY WAVE AMPLITUDE SPECTRA — FAR-FIELD P WAVE
1 HZ SPECTRAL AMPLITUDES AT $\tau = 20°$

Identifier	Material	Depth (km)	Spectral Amplitude
13	Granite	Spherically Symmetric	1.8
1	"	0.159	1.8
2	"	0.207	2.1
3	"	0.253	1.5
4	Dry Sandstone	0.159	0.60
5	"	0.207	0.65
6	"	0.253	0.72
7	Weak Dry Sandstone	0.207	1.4
14	Wet Sandstone	Spherically Symmetric	1.7
8	"	0.053	1.3
9	"	0.159	2.1
10	"	0.207	2.8
11	"	0.253	2.7
12	"	0.531	2.5

TABLE 3.1.3

SURFACE WAVE AMPLITUDE SPECTRA (0.05 Hz)

Identifier	$P(\tau=20°)$	$S(\tau=20°)$	$P(\tau=70°)$	$S(\tau=70°)$
13	1.3	-	1.3	-
1	2.9	2.0	1.1	5.4
2	3.2	5.7	1.2	15.6
3	3.3	0.9	1.2	2.7
4	6.5	1.1	2.4	2.8
5	7.1	5.0	2.6	1.4
6	5.6	5.7	2.1	1.6
7	10.6	0.95	3.9	2.4
14	2.0	-	2.0	-
8	2.2	1.7	0.78	4.6
9	10.1	7.4	3.7	20.2
10	21.3	13.6	7.7	37.8
11	14.4	22.0	5.2	60.1
12	13.7	11.8	5.0	32.5

TABLE 3.1.4

SOURCE REGION CRUSTAL MODEL

Depth (km)	Thickness (km)	α(km/sec)	β(km/sec)	ρ(g/cm³)
1.0	1.0	Granite, Wet or Dry Sandstone		
1.7	0.7	4.7	2.7	2.6
2.7	1.0	5.4	2.8	2.7
4.0	1.3	5.8	3.45	2.8
20.0	16.0	6.0	3.50	2.8

TABLE 3.1.5

RECEIVER REGION CRUSTAL STRUCTURE

Depth (km)	Thickness (km)	α(km/sec)	β(km/sec)	ρ(km/sec)
2.58	2.58	3.67	2.31	2.40
4.84	2.26	5.42	3.27	2.60
11.61	6.77	5.80	3.45	2.60
20.0	8.39	6.00	3.50	2.80

this case we took the distance to be $\Delta = 36°$ which is beyond the upper mantle triplications and the upper mantle response is essentially a constant geometric spreading factor.

4. The response of the receiver crustal model (Table 3.1.5) is included. In this case the receiver crust has little effect other than scaling the seismogram.

5. The response is convolved with an operator representing the attenuation and dispersive properties of the earth. For these calculations we took $t* = 0.7$ (t* is the ratio of travel time to the effective path attenuation factor, Q).

6. The ground motion is convolved with the response of a standard short period seismograph system.

The synthetic seismograms are shown in Figures 3.1.8 - 3.1.10. The cycle from which m_b is measured is indicated on each record by a bar. The m_b values and the period of the m_b cycle are tabulated in Table 3.1.6. The m_b is computed from

$$m_b = \log \frac{A}{T} + 3.32 \, , \tag{3.1.3}$$

where T is the period tabulated, A is the peak-to-peak amplitude of the indicated cycle corrected for the instrument response at the period T, and the constant 3.32 is the appropriate distance correction factor. Recall that for all the seismogram calculations there is no free surface near the source.

It is interesting to examine how the m_b scales with the far-field displacement spectra discussed in Section 3.1.4. To first order we expect to have [Bache, et al., 1976],

$$m_b \approx \log \left(\alpha_s^2 \, \hat{u} \right) \, , \tag{3.1.4}$$

22
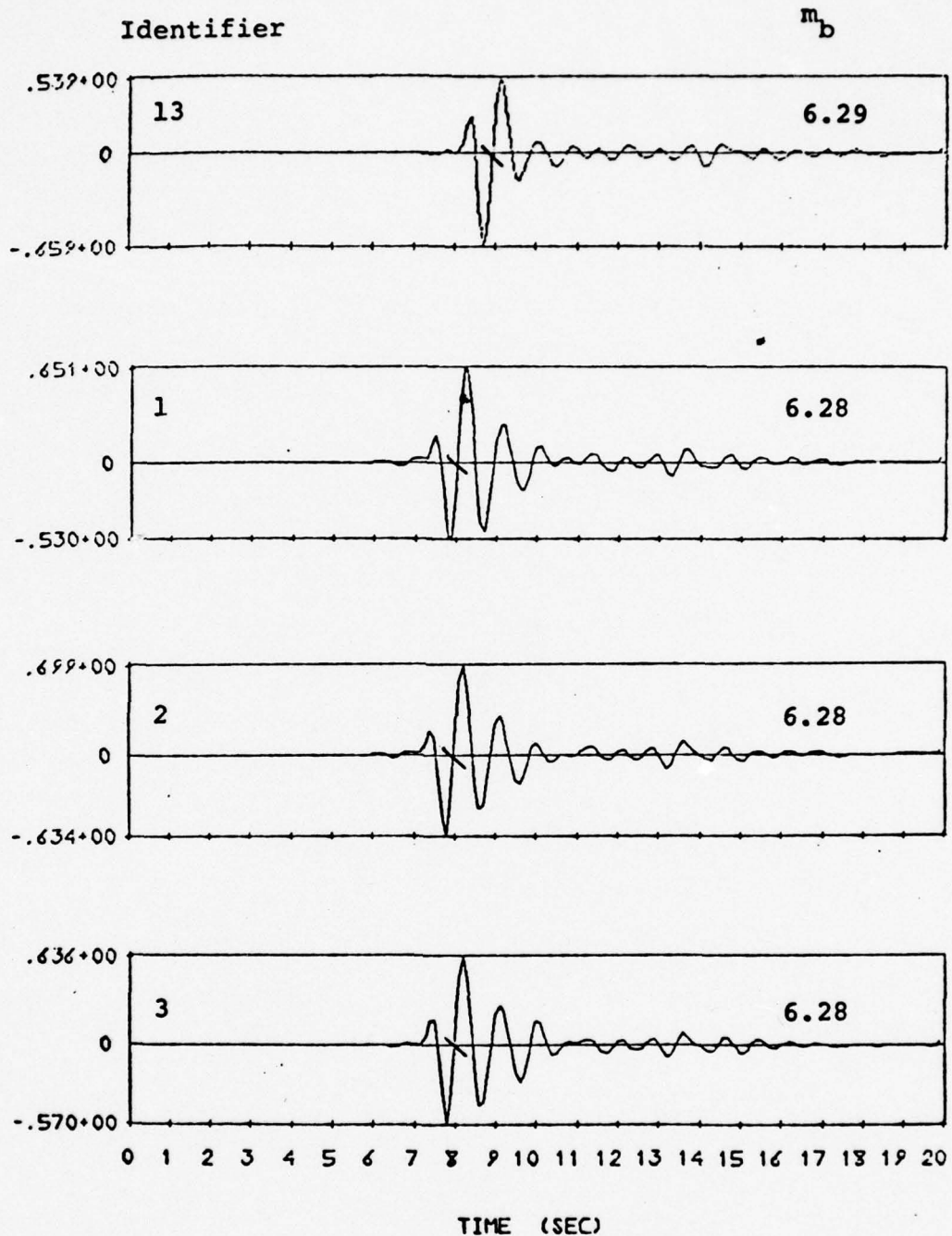
Figure 3.1.8. Synthetic short period seismograms for one spherically symmetric and three cratering calculations in granite. The numbers to the left are ground motion in microns at 1 Hz.
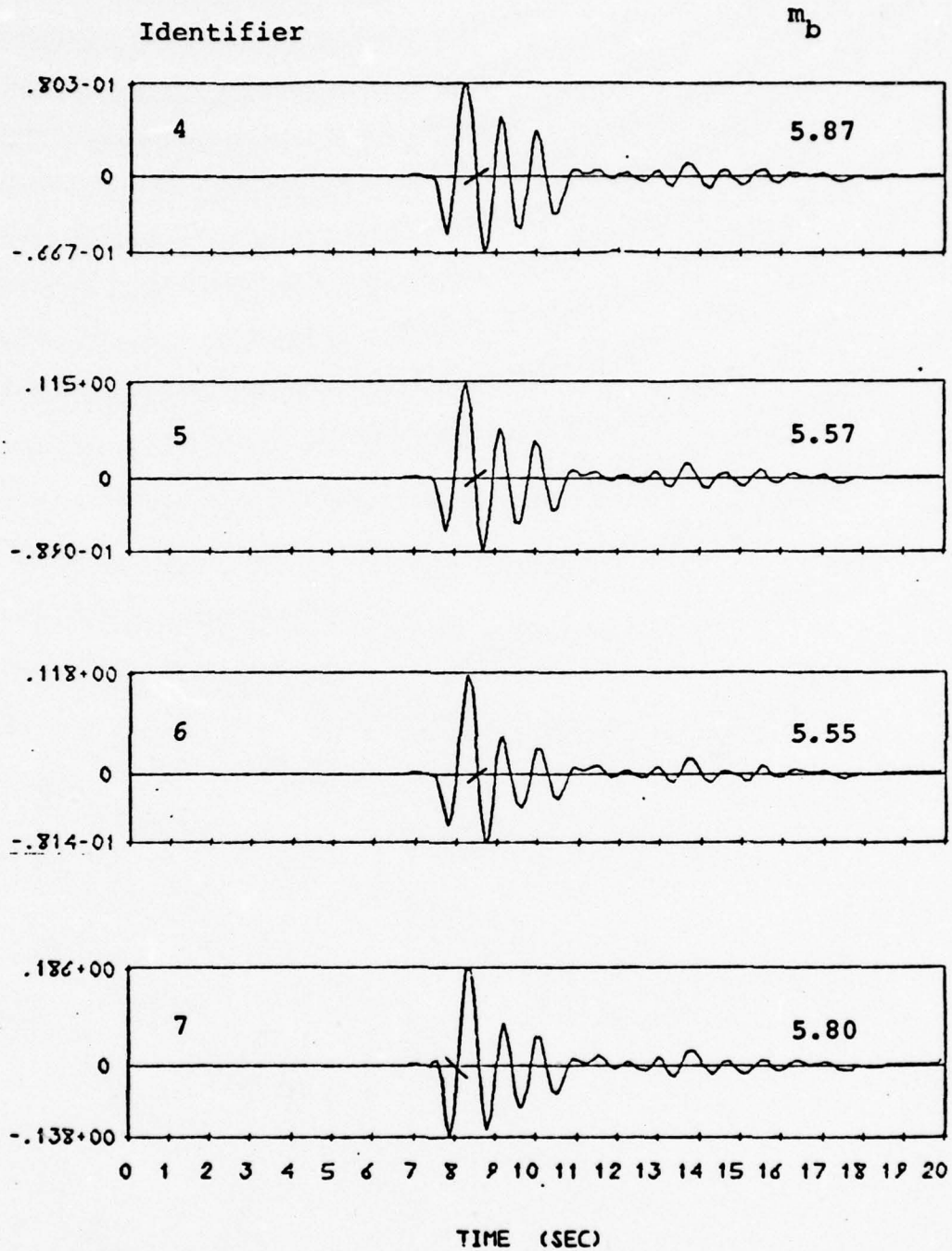
Figure 3.1.9. Synthetic short period seismograms for four cratering calculations in dry sandstone. The numbers to the left are ground motion in microns at 1 Hz. Note that the apparent first motion is downward. This appears to be a consequence of the constitutive properties of the dry sandstone.

24

R-3108
m_b
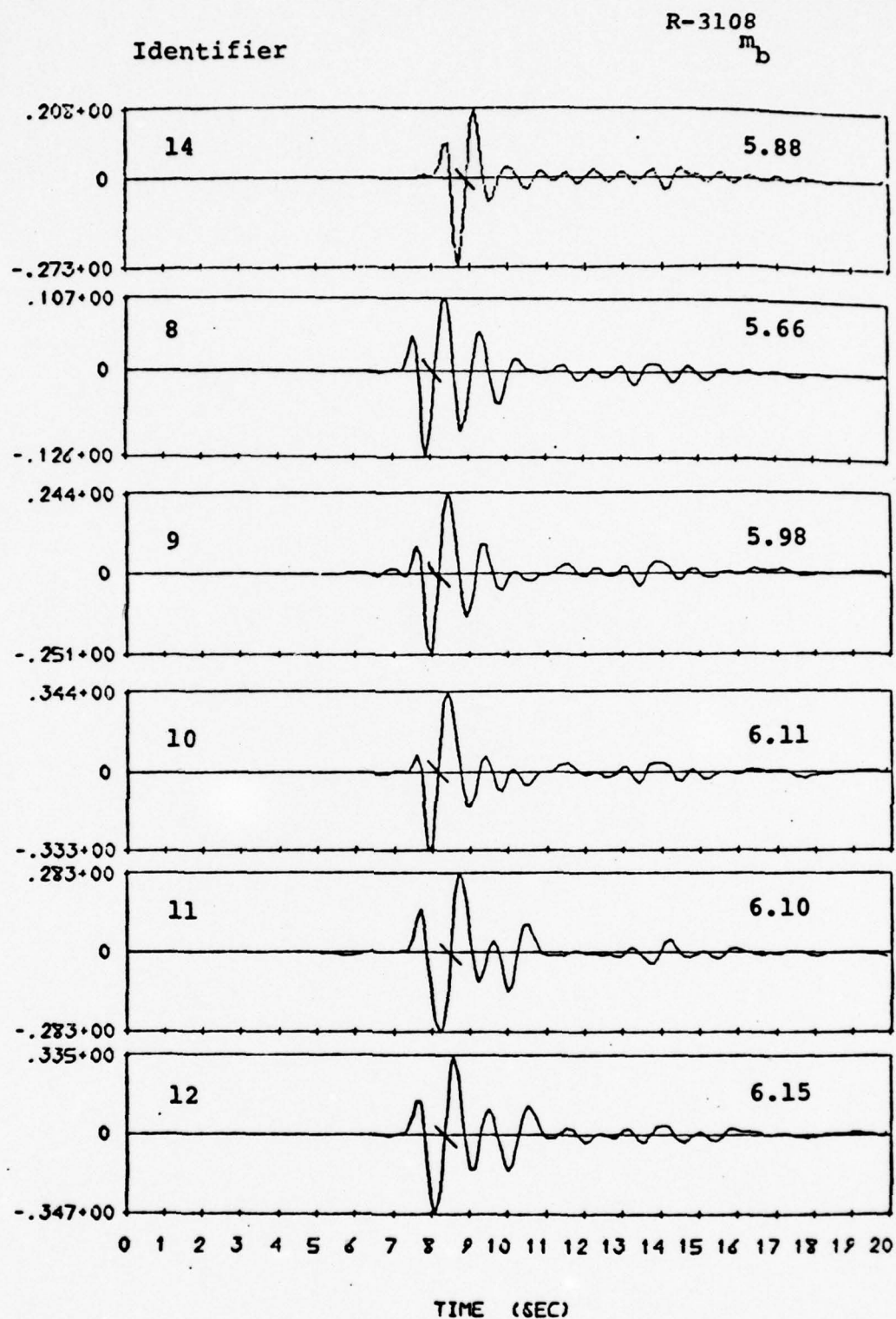
Figure 3.1.10. Synthetic short period seismograms for one spherically symmetric and five cratering calculations in wet sandstone. The numbers to the left are ground motion in microns at 1 Hz.

25

TABLE 3.1.6

SUMMARY OF m_b VALUES FOR ATI CRATERING CALCULATIONS

Identifier	Depth	m_b	m_b Period	Normalized $(A/T)/\alpha_s^2\hat{u}$
Granite				
13	Spherically Symmetric	6.29	0.81	0.93
1	0.159	6.28	0.78	0.85
2	0.207	6.34	0.82	0.73
3	0.253	6.28	0.80	1.01
Dry Sandstone				
4	0.159	5.48	0.96	0.96
5	0.207	5.57	0.88	1.09
6	0.253	5.55	0.86	0.94
7 (weak)	0.207	5.80	0.93	0.86
Wet Sandstone				
14 (1-D)	Spherically Symmetric	5.88	0.79	1.00
8	0.053	5.66	0.94	0.79
9	0.159	5.98	0.92	1.02
10	0.207	6.11	0.92	1.05
11	0.253	6.10	1.03	1.05
12	0.531	6.15	0.99	1.27

where $\hat{u}$ is the displacement spectrum at the controlling frequency and α_s is the P wave velocity at the source. Using the values of α_s from Table 3.1.1 and $\hat{u}$ (1 Hz) from Table 3.1.2, we normalize the amplitudes and scale to the value for calculation 14. The normalized scaled amplitudes are tabulated in the last column of the table. We see that all values are within $\pm$ 27 percent of the normalized amplitude for calculation 14. Further, eleven of the fourteen are scaled to within 15 percent by (3.1.4). The discrepancies are mainly attributed to the fact that we are normalizing to the spectral amplitude at 1 Hz while the frequencies controlling the seismogram amplitudes range from 0.97 - 1.32 Hz. From Figures 3.1.2 - 3.1.7 we see that the P wave spectra are complex and rapidly changing in this region.

3.1.6 Surface Wave Amplitude, M_s

In this section we present our synthetic long period seismograms for the fourteen ATI sources and give the M_s values for each. The synthetic seismogram calculations include the following elements:

1.   The method for the surface wave calculations is described by Harkrider [1964] and Harkrider and Archambeau [1977]. The same equivalent elastic source formulation used for the body waves is used for the surface waves. Once again, only the downgoing waves from the source are included in the calculations.

2.   Two crustal models are used for the path, one for the very near source region and one for the remainder of the path to the receiver. The average path model is one proposed for North America by McEvilly [1964]. The only difference between the models is that the top three kilometers of the

27

source region crustal model is replaced by the ATI granite, wet or dry sandstone, depending on the source material. For the long periods controlling teleseismic M_s the reflection coefficient for Rayleigh waves passing across the boundary between the source and average path crustal model is close to unity.

3.   The ground motion is convolved with the response of an LRSM long period seismometer. A Q operator which has only a minor effect is also included. The Q model is that of Tryggvason [1965].

4.   The seismograms were synthesized at a range of 3000 km. The M_s was computed using the formulas of Marshall and Basham [1972]. For this range the formula reduces to

$$M_s = \log A + 1.38 + P(T)$$

where A is the maximum amplitude (zero-to-peak) of the signal with period near 20 seconds and P(T) is a period dependent path correction tabulated by Marshall and Basham [1972]. The correction is quite small for periods near 20 seconds.

The vertical component Rayleigh wave synthetic seismograms are shown in Figures 3.1.11 - 3.1.13. Two seismograms are shown for the spherically symmetric contained explosions in granite and wet sandstone (cases 13 and 14). In one of these (13b, 14b) only the downward waves are included in the calculation. The seismograms are then the analog of the case 13 and 14 body wave seismograms of Figures 3.1.8 and 3.1.10. Since the M_s is relatively insensitive to depth for contained explosions (unlike m_b which is strongly affected by the pP phase), we also computed seismograms for fully contained explosions at a depth of 200 meters. The seismograms are given as cases 13a and 14a.

28

Figure 3.1.11. Vertical component Rayleigh wave seismograms for a spherically symmetric and three cratering explosions in granite. The numbers at the left are displacement in microns at 25 seconds.

Identifier M_s

TIME (SEC)

Figure 3.1.12.   Vertical component Rayleigh wave seismograms
                 for four cratering explosions in dry sand-
                 stone. The numbers at the left are dis-
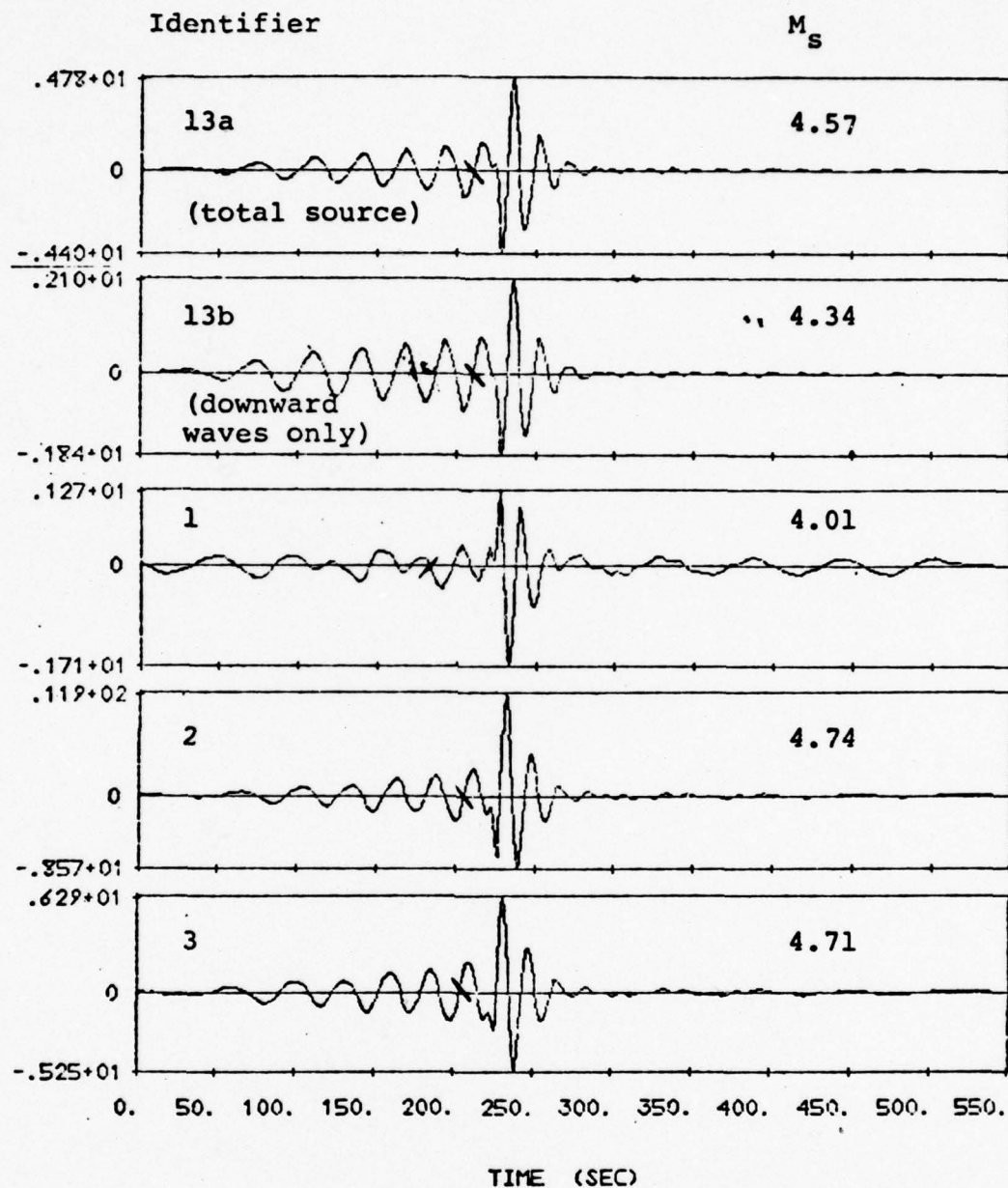   placement in microns at 25 seconds.

30
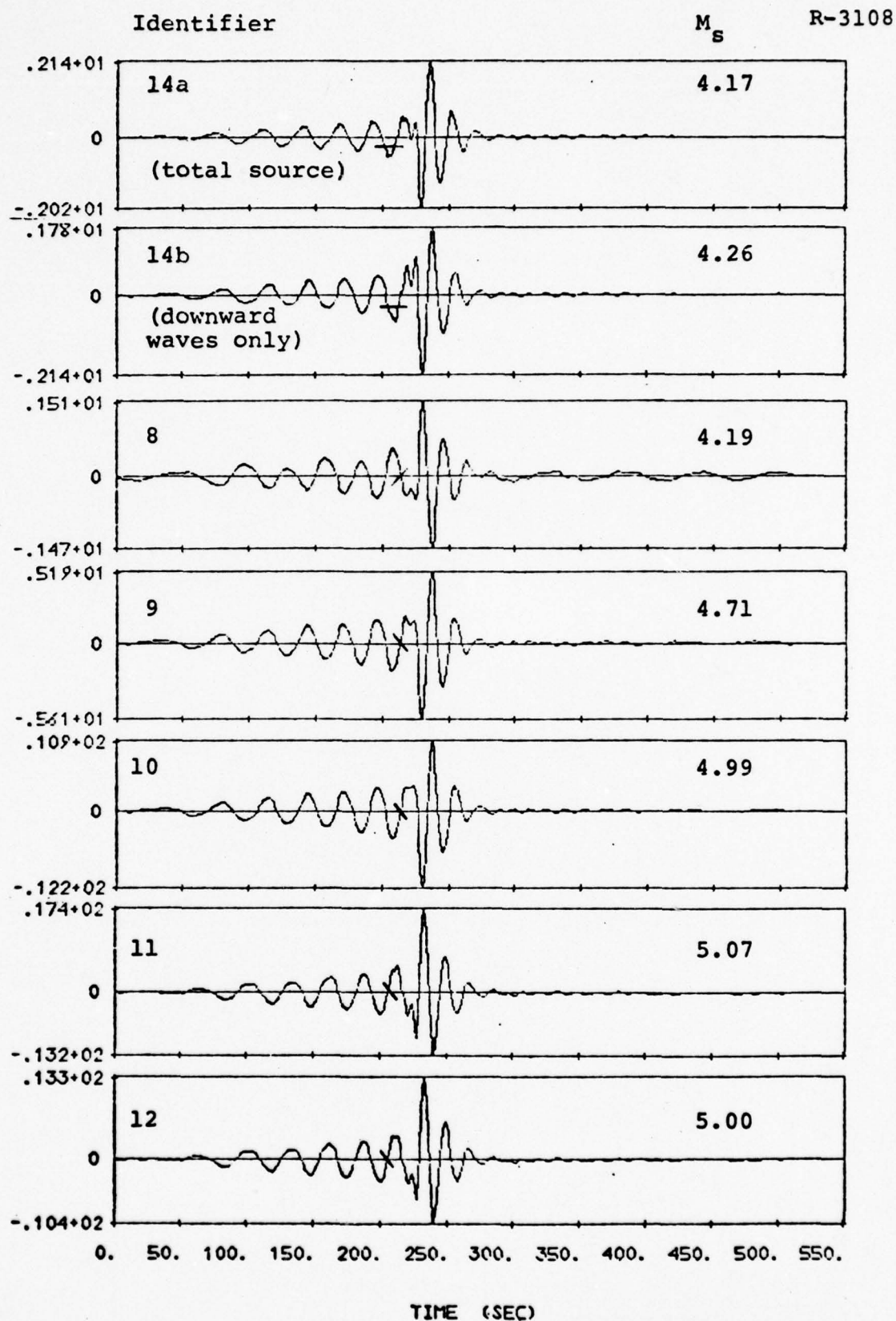
Figure 3.1.13.   Vertical component Rayleigh wave seismograms
for a spherically symmetric and five cratering
explosions in wet sandstone.   The numbers at
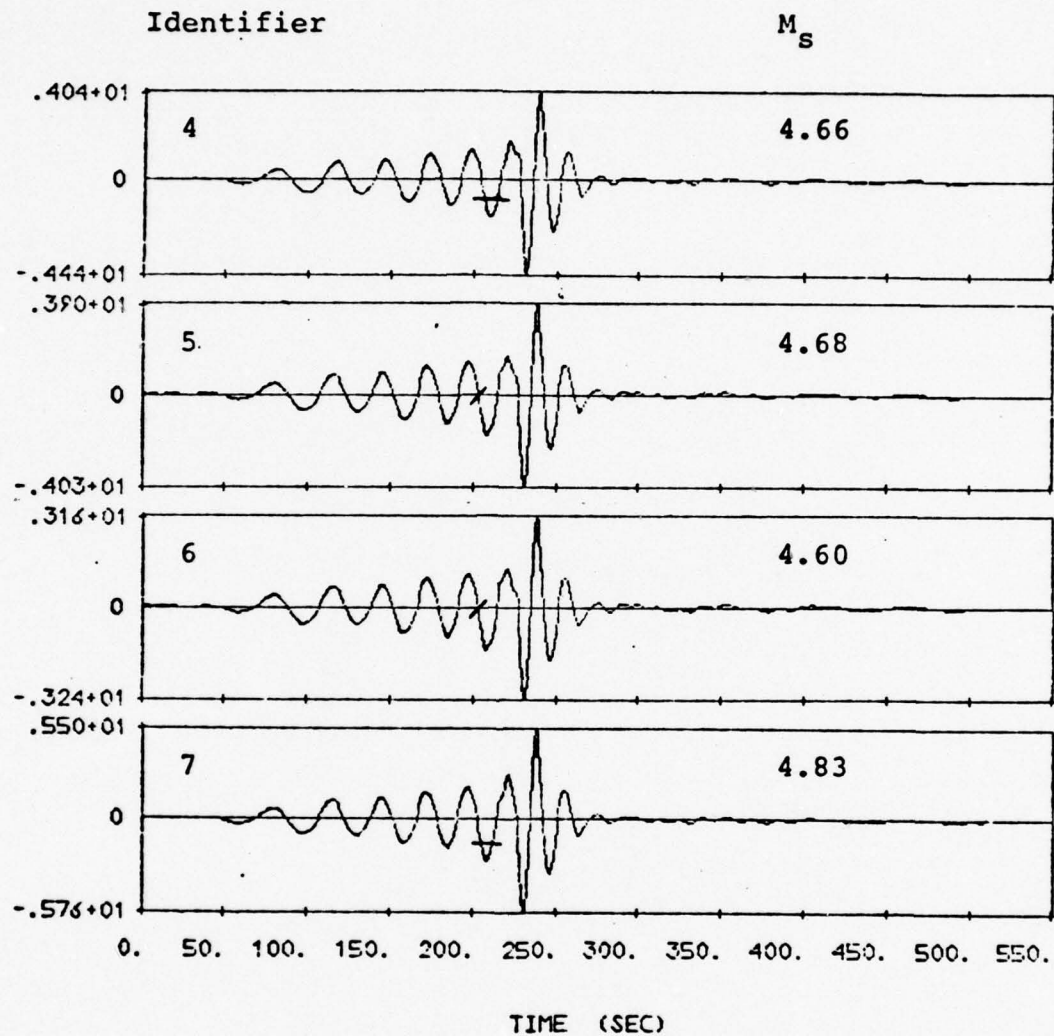the left are displacement in microns at 25
seconds.

TABLE 3.1.7

SUMMARY OF M_s VALUES FOR ATI CRATERING CALCULATIONS

Identifier	Depth (km)	M_s	M_s Period	Log Spectral Amplitude, $\log \hat{A}$ (20 sec)	$M_s - \log \hat{A}$
Granite					
13A	1-D Total Source	4.57	20.1	1.92	2.65
13B	1-D Down Waves Only	4.34	21.5	1.62	2.72
1	0.159	4.01	20.0	1.30	2.71
2	0.207	4.95	23.6	2.25	2.70
3	0.253	4.72	21.8	2.03	2.69
Dry Sandstone					
4	0.159	4.66	22.0	1.92	2.74
5	0.207	4.68	22.7	1.92	2.76
6	0.253	4.60	22.5	1.83	2.77
7 (weak)	0.207	4.83	22.0	2.07	2.76
Wet Sandstone					
14A	1-D Total Source	4.17	22.8	1.52	2.65
14B	1-D Down Waves Only	4.26	20.0	1.53	2.73
8	0.053	4.19	21.2	1.43	2.76
9	0.159	4.71	21.2	2.02	2.69
10	0.207	4.99	19.3	2.35	2.64
11	0.253	5.07	20.1	2.44	2.63
12	0.531	5.00	19.8	2.34	2.66

The important data from the seismograms of Figures 3.1.11 - 3.1.13 are summarized in Table 3.1.7. The phase at which the amplitude for M_S was measured is indicated on the seismograms of Figures 3.1.11 - 3.1.13 by a bar. The period of this phase is given in the table. Also listed in the table is the spectral amplitude of the true ground motion at a period of 20 seconds. The difference between M_S and $\log \hat{A}$ indicates the consistency to which the M_S measurement represents a true measurement of the energy at frequencies in this range. These differences are tabulated in the last column of Table 3.1.7. We see that the M_S values are quite consistent with the spectral measurements with the spread between the maximum and minimum values being 0.14 M_S units.

3.1.7 Contribution of the Ejecta Fallback to Teleseismic Ground Motion

In carrying out the cratering calculations, ATI also tracked the ejecta and computed the surface loading due to its fall back to the free surface. The resulting surface loading consists of an axisymmetric distribution of normal and shear stresses on the surface. If we Fourier transform all transient quantities, the free surface boundary conditions are:

$$P_{zz}(r,\phi,0,\omega) = P_0(r,\omega) \ ,$$

$$\text{(3.1.5)}$$

$$P_{zr}(r,\phi,0,\omega) = Q_0(r,\omega) \ ,$$

where P_{zz} and P_{zr} are the Fourier transformed normal and shear stress components in a cylindrical coordinate system. The P_0 and Q_0 are the applied stress distributions.

The elastic waves generated by loading of the form (3.1.5) on the free surface of a multilayered halfspace can be worked out analytically using techniques similarly applied by Harkrider [1964] or Bache and Harkrider [1976] for the

33

buried source. The theory is presented in detail in our forthcoming topical report. In this report we will simply give the results.

In computing surface waves for the ejecta we found the maximum amplitude of the generated surface waves to be 1-2 orders of magnitude lower than for the surface waves from the contained portion of the explosion. The amplitude of the displacement spectrum falls off rapidly for frequencies above 0.1 Hz so the contribution to the body waves is quite a bit less. We concluded, therefore, that the ejecta contribution to m_b and M_s could safely be ignored.

3.2   BODY WAVE ATTENUATION PROPERTIES FOR SELECTED TRAVEL PATHS

3.2.1 Introduction

The frequency content of the first few cycles of explosion P waves recorded at teleseismic distances is primarily controlled by the shape of the source function, the delay time between P and pP, and the anelastic properties ($t^* = T/Q$, where T is the travel time and Q is the average path material quality factor) of the source-receiver propagation path. The primary objective of this particular study is to determine variations in t^* between U.S. and USSR test sites and, in particular, the effect that this variation produces on yield estimates from teleseismic P waves. As a first step toward a solution to this problem, we have compared the frequency content of a large population of NTS and Eurasian explosions at several recording stations where we have previous experience in predicting explosion P waves.

3.2.2 Station Locations and Experimental Data

Short-period seismograms of explosion P waves were obtained from two different sources for this experiment. One source was the Palmer network of seismic stations located throughout Alaska and the Aleutian Islands. The names, codes and locations of four of the Palmer stations used in this experiment are given in Table 3.2.1.

The second source of data was two stations of the Atomic Energy Detection System (AEDS) network, hereafter referred to as Sites A and B, located at teleseismic distances from the NTS and Eurasian test sites.

Using these explosion seismograms, the dominant periods of the "b" and "d" phases of the short-period P waves were measured for each event. Examples of these two measurements, T_b and T_d, are shown in Figure 3.2.1.

TABLE 3.2.1

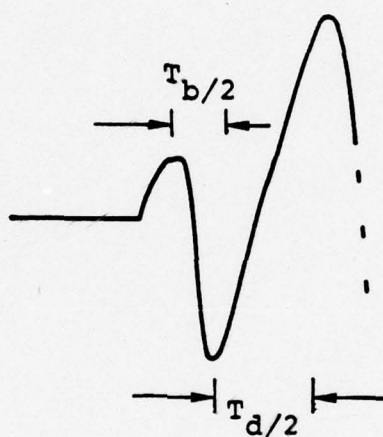| Station Name	Code	Location
Adak Observatory, Aleutians	ADK	51°53'01"N 176°41'04"W
Arctic Valley, Palmer	PMS	61°14'41"N 149°33'38"W
Gilmore Creek, Fairbanks	GIL	64°58'30"N 147°29'42"W
Kodiak Island	KDC	57°44'52"N 152°29'30"W

Figure 3.2.1 Sketch of a typical explosion P-wave with
dominant period measurements, T_b and T_d,
indicated.

As can be seen in Figure 3.2.1, T_b is based on a half-cycle within the first portion of the P wave while T_d is usually based on a later occurring half-cycle corresponding to the maximum amplitude excursion within the first three or four cycles of the P wave. For events located in the same source region and recorded at a common station the b phase has been found to be a more precise measure of explosion coupling than the d phase [Bache, et al., 1975]. This is attributed to the fact that the b portion of an explosion P wave is less contaminated by later arriving phases (i.e., pP, mantle arrivals).

3.2.3 Results of Data Analysis

The period measurements, T_b and T_d, are plotted in Figures 3.2.2 through 3.2.15 versus estimates of explosion yields for a large population of NTS and Eurasian events. The yield estimates are based on body wave magnitude determinations and are taken from Klepinger [1974] and Alewine, et al. [1975]. The results of this analysis are categorized and presented according to type of measurement (T_b or T_d), recording station and event source region.

Some comments based on the explosion data from the Palmer stations, PMS (Figures 3.2.2-3.2.5), KDC (Figures 3.2.6-3.2.7) and ADK (Figures 3.2.8-3.2.9) are the following:

1. The dominant periods of both the b and d phases for presumed explosions in east Kazakhstan are shorter than the corresponding periods for NTS events in the same yield range. Mean values of T_b and T_d are shorter by approximately 0.5 sec at PMS and KDC, and 0.2 sec at ADK.

2. The scatter in the observed T_b values is between a factor of 1-1/2 and 2 less than the scatter in T_d values.
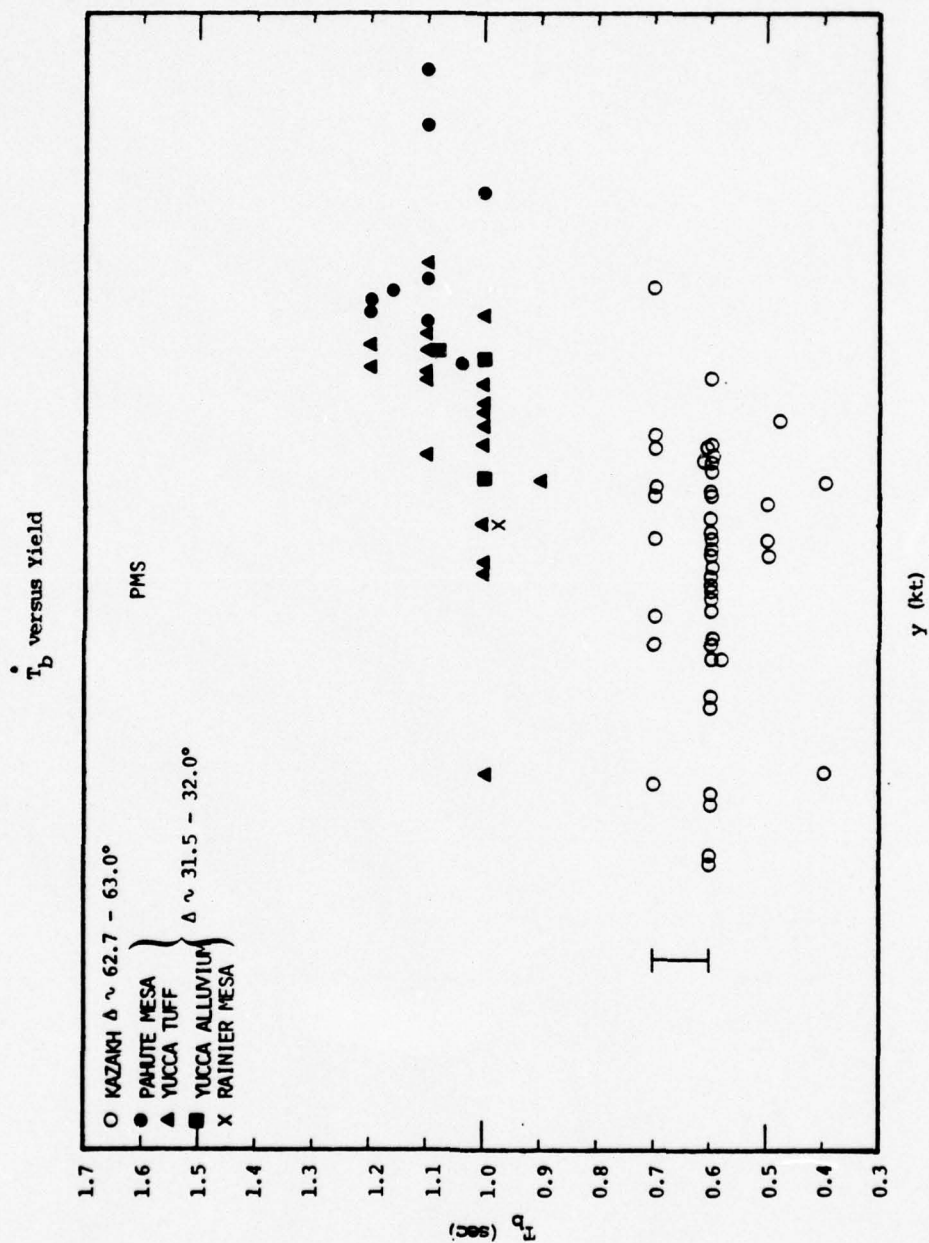
Figure 3.2.2. T_b versus yield for large population of NTS and Eurasian (east Kazakhstan) events recorded at the PMS station of the Palmer network.
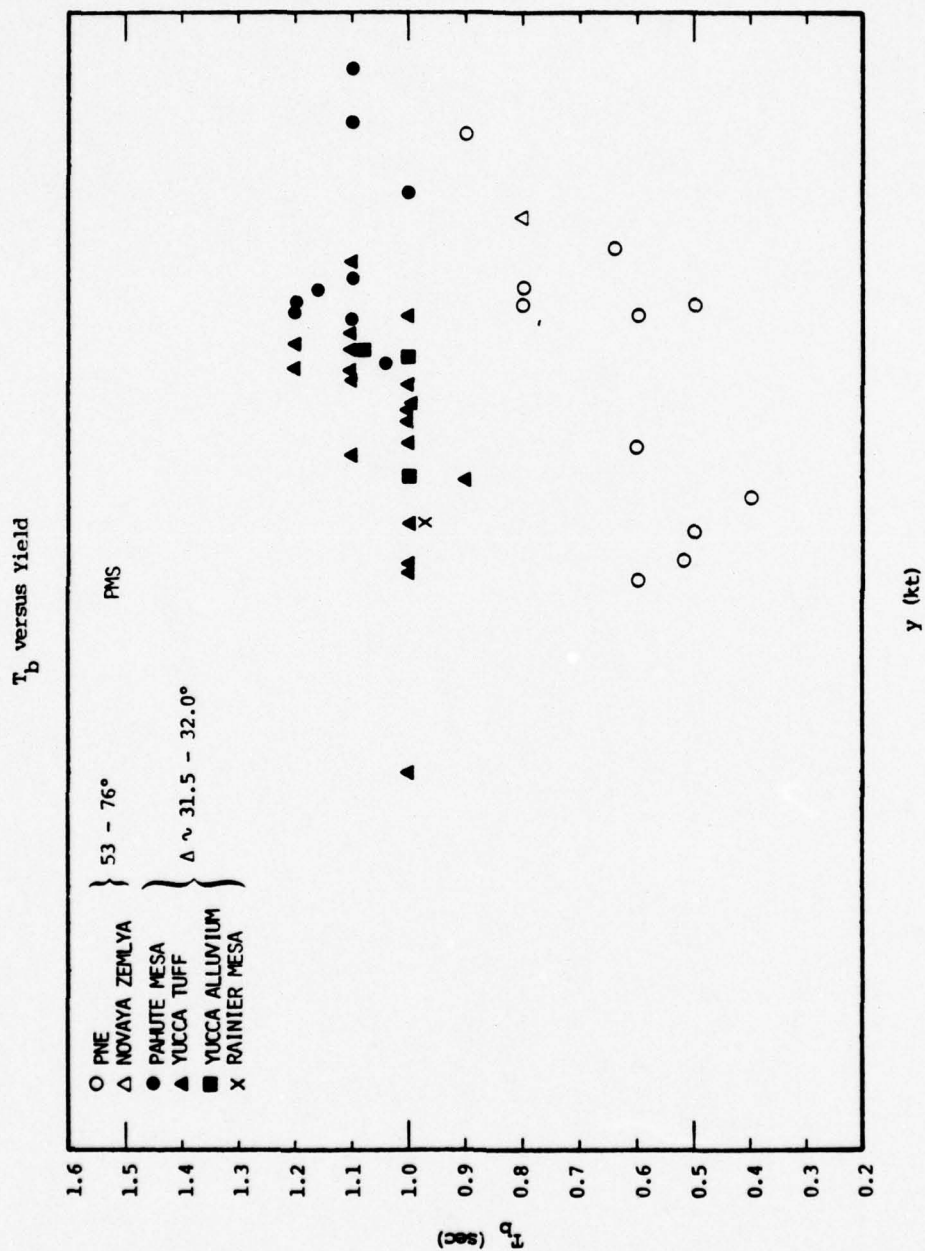
Figure 3.2.3. T_b versus yield for large population of NTS and Eurasian (PNE's and Novaya Zemlya) events recorded at PMS.

40

Figure 3.2.4. T_d versus yield for same event population as in Figure 3.2.2.

Figure 3.2.5. T_d versus yield for same event population as in Figure 3.2.3.

42

Figure 3.2.6. T_b versus yield for NTS (Pahute Mesa) and Eurasian (east Kazakhstan) events recorded at the KDC station of the Palmer network.

43
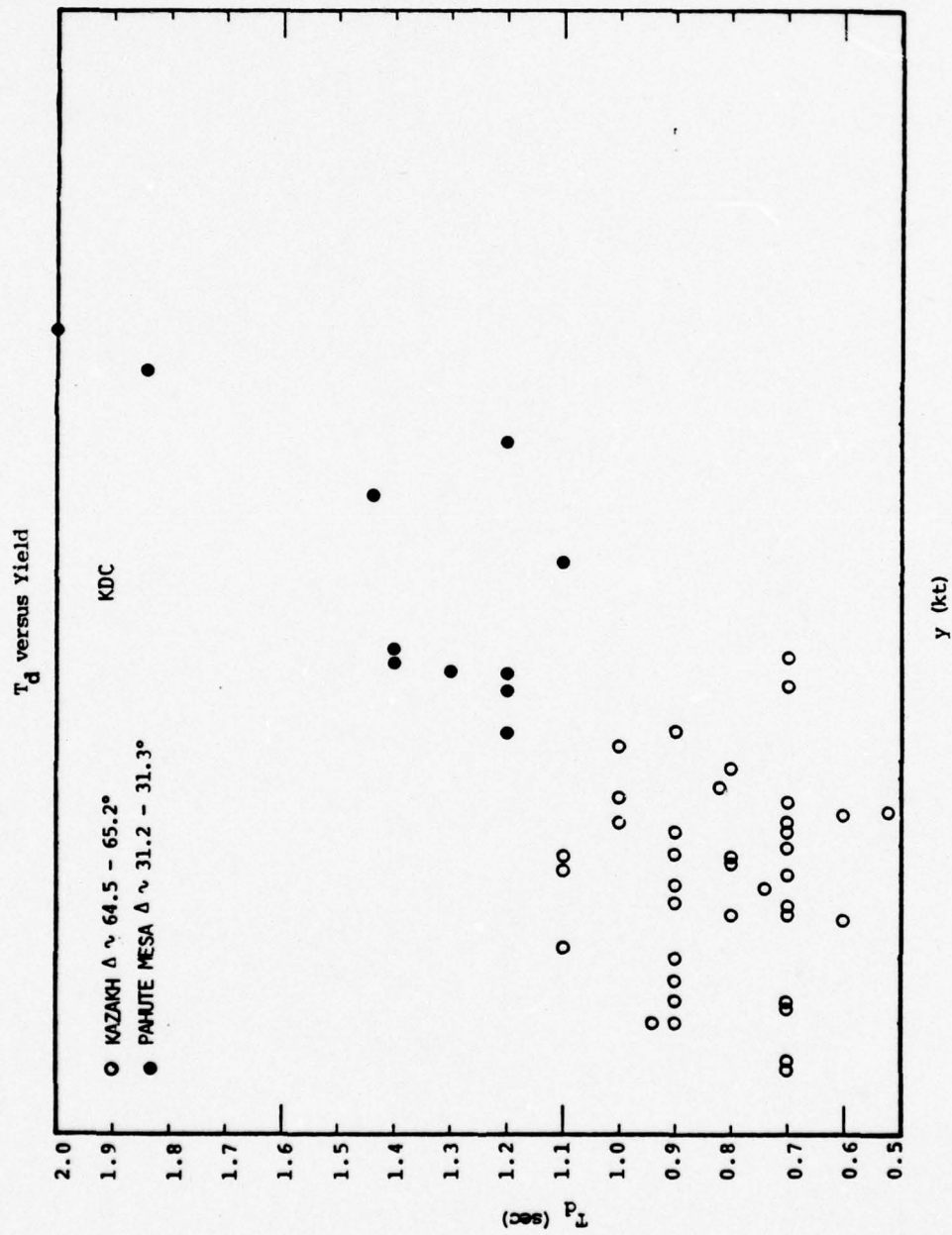
Figure 3.2.7. T_d versus yield for same event population as in Figure 3.2.2.

44
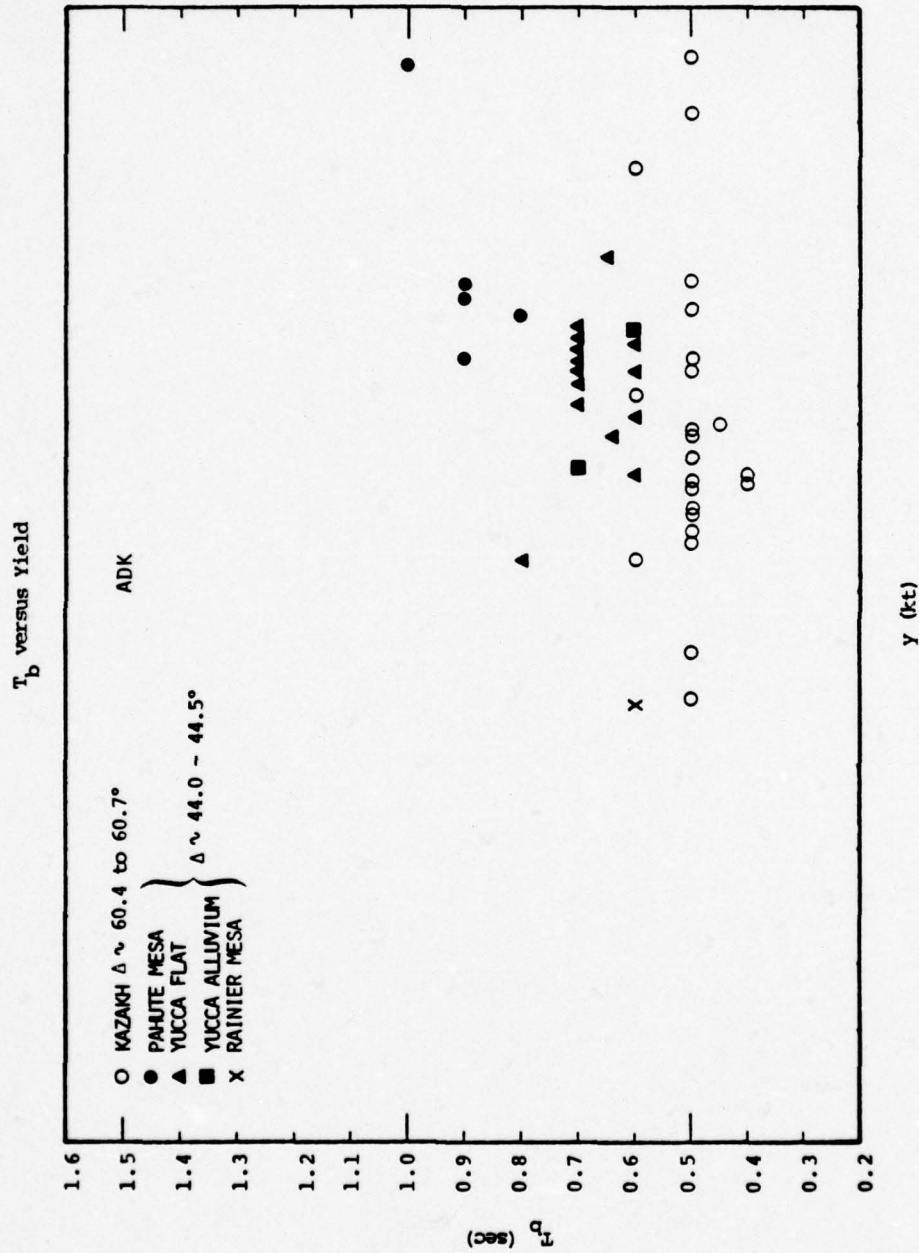
Figure 3.2.8. T_b versus yield for NTS and Eurasian (east Kazakhstan) events recorded at the ADK station of the Palmer network.

45

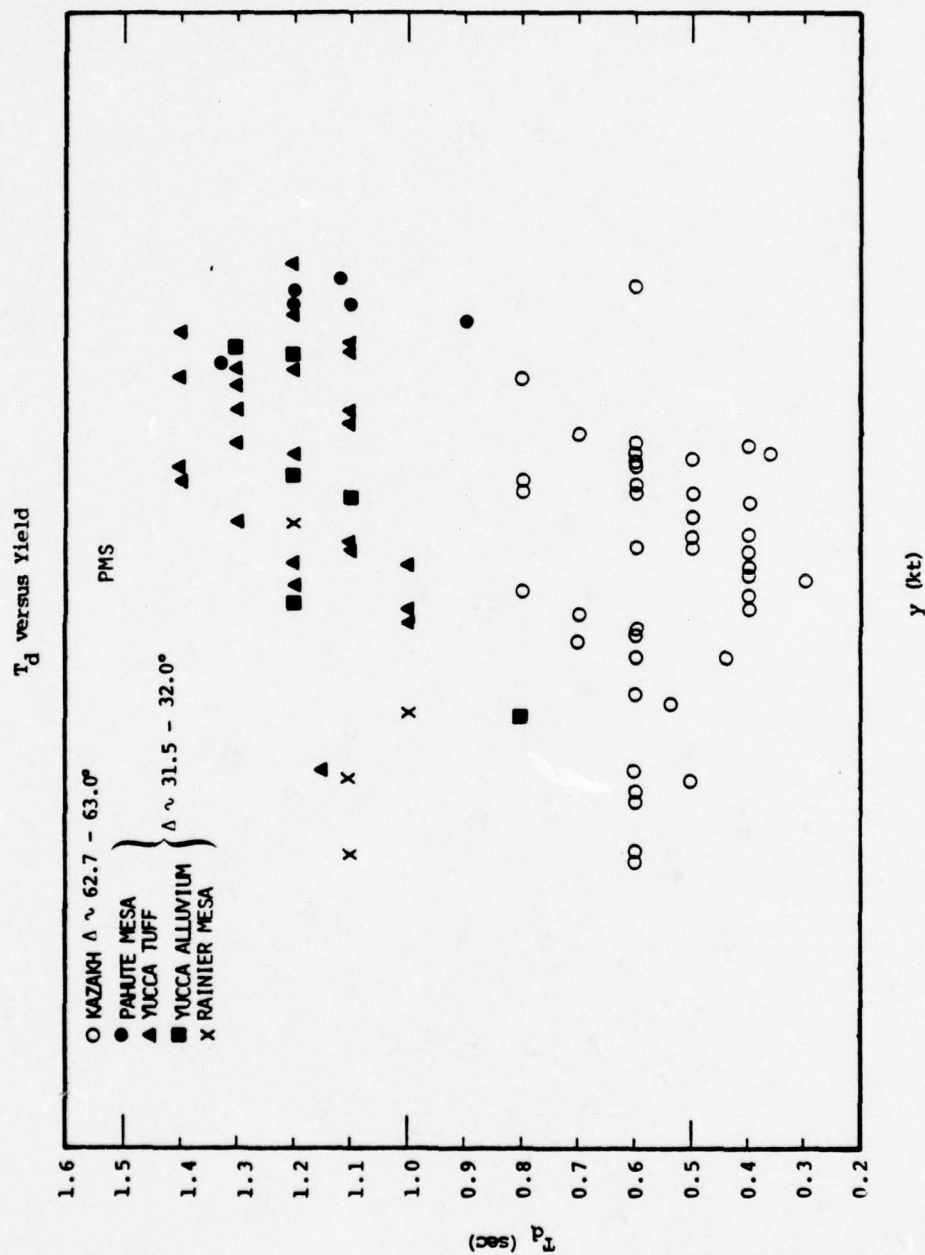Figure 3.2.9. T_d versus yield for same events as in Figure 3.2.2.

T_b versus Yield

GIL

Legend:
- O KAZAKH $\Delta \sim 59.9 - 60.3°$
- ● PAHUTE MESA
- ▲ YUCCA TUFF
- ■ YUCCA ALLUVIUM $\left. \right\} \Delta \sim 33.2 - 33.8°$
- X RAINIER MESA

T_b (sec)

1.7 1.6 1.5 1.4 1.3 1.2 1.1 1.0 0.9 0.8 0.7 0.6 0.5 0.4 0.3

Y (kt)
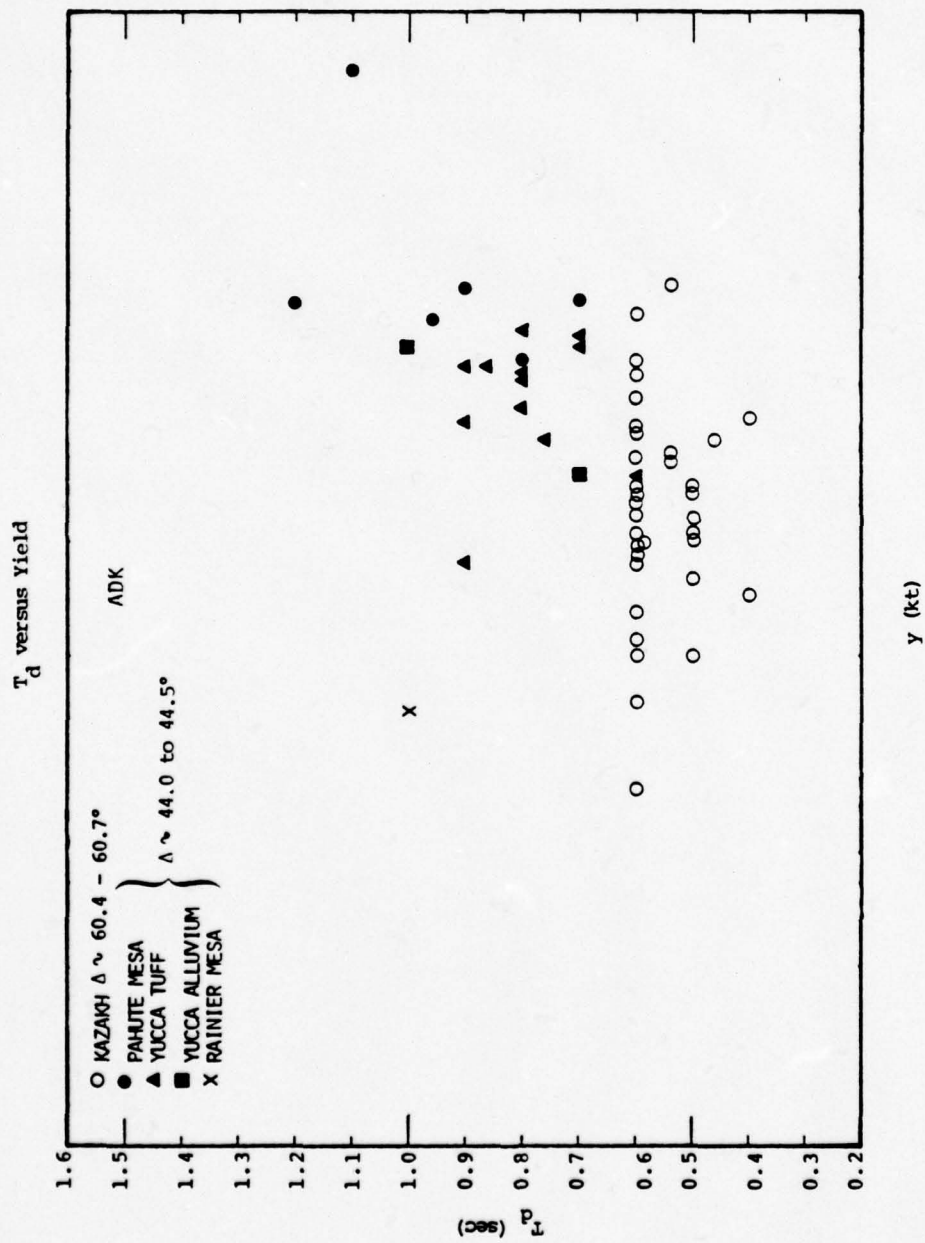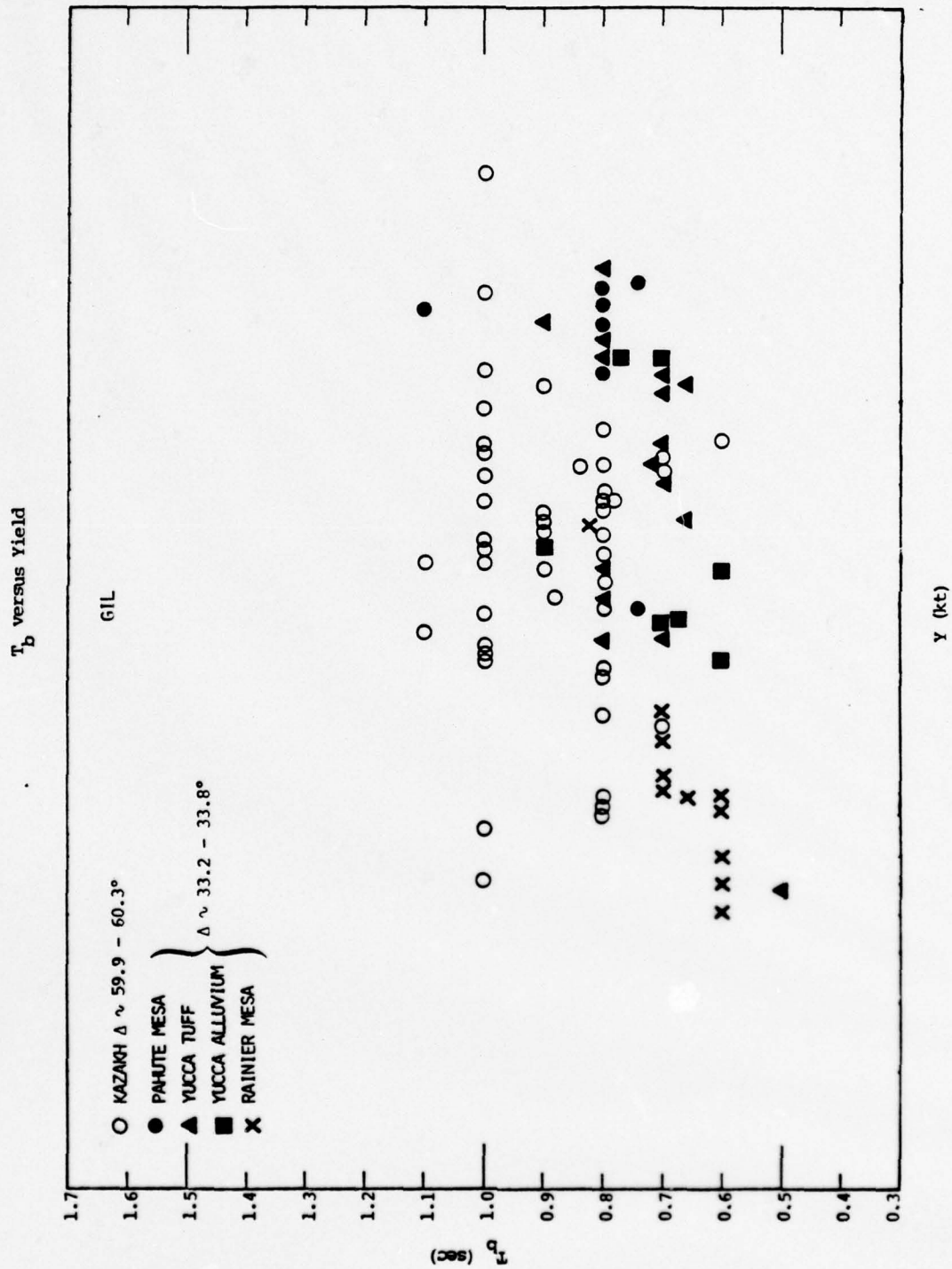
Figure 3.2.10. T_b versus yield for NTS and Eurasian (east Kazakhstan) events recorded at the GIL station of the Palmer network.
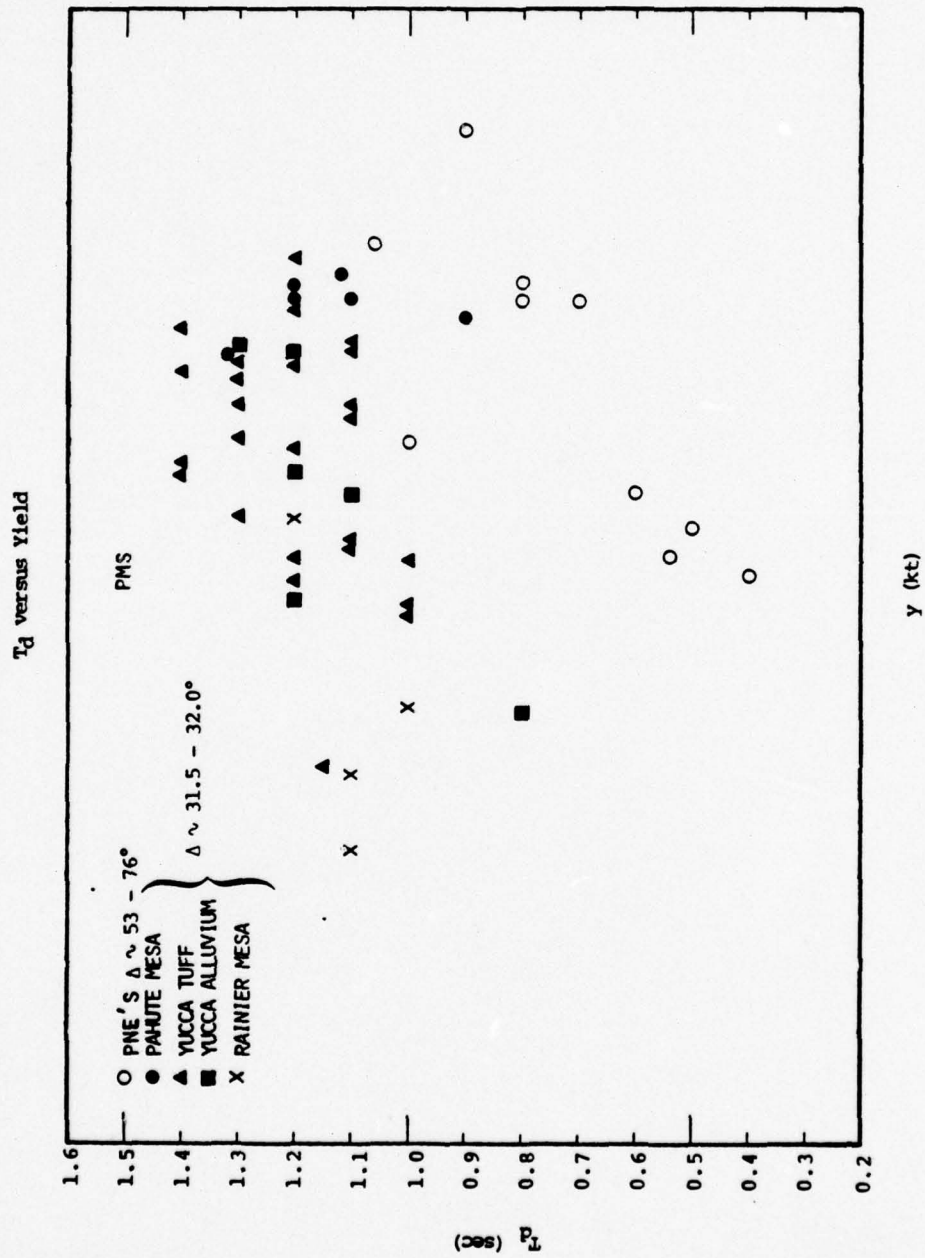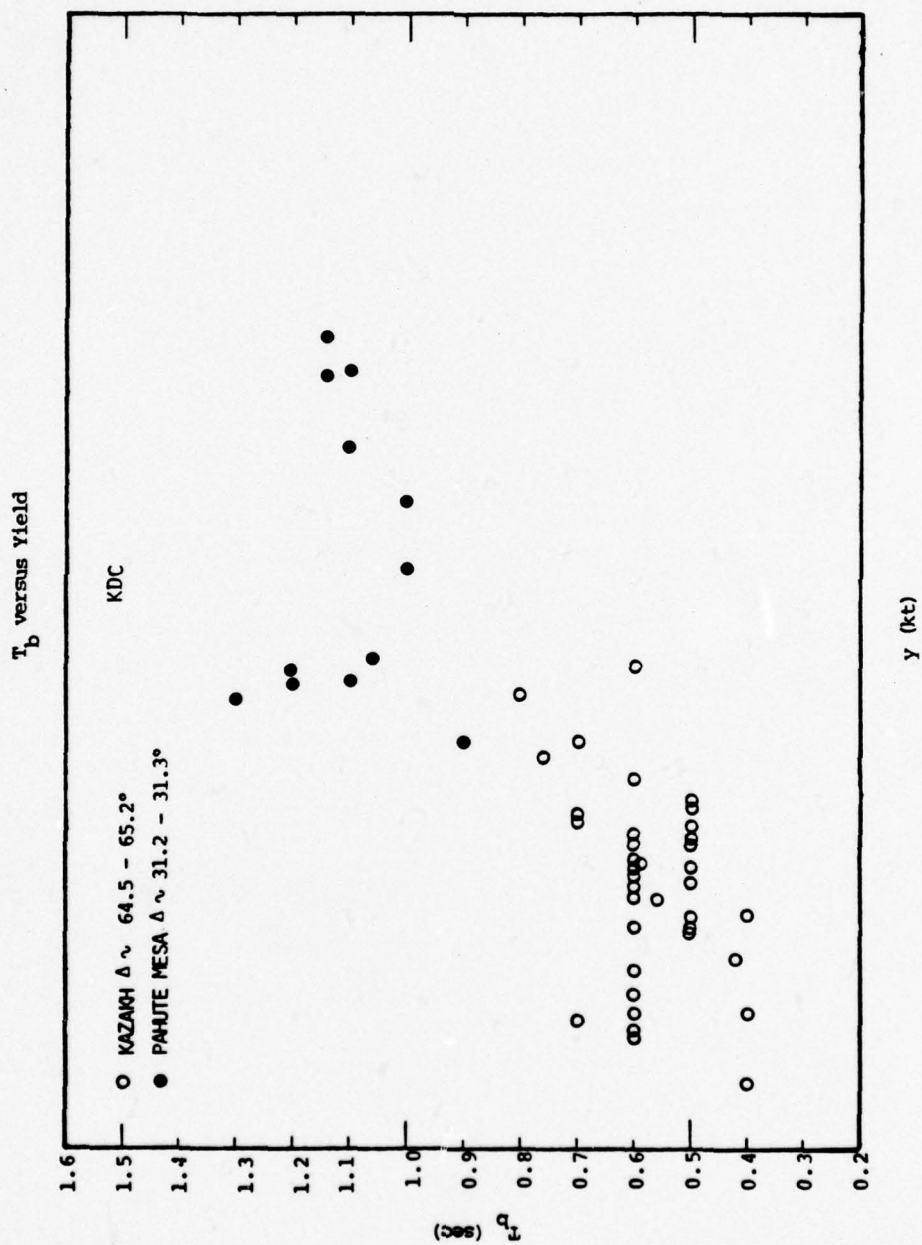
T_b versus Yield

GIL

$\Delta \sim 43 - 73°$

$\Delta \sim 31.5 - 32°$

○ PNE
● PAHUTE MESA
△ NOVAYA ZEMLYA
▲ YUCCA TUFF
■ YUCCA ALLUVIUM
✕ RAINIER MESA

1.5
1.4
1.3
1.2
1.1
1.0
0.9
0.8
0.7
0.6
0.5
0.4
0.3
0.2
0.1

T_b (sec)

Y (kt)
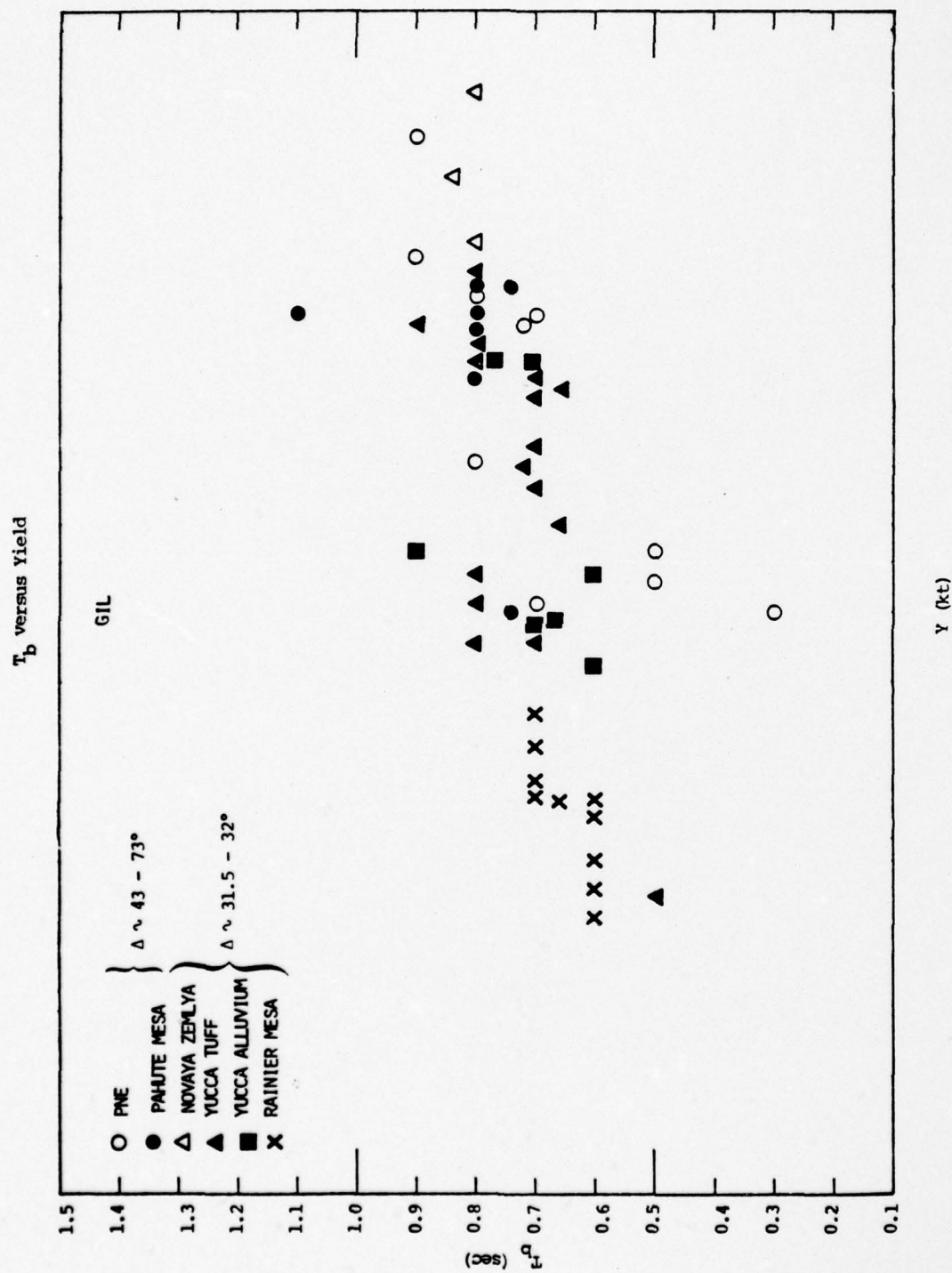
Figure 3.2.11. T_b versus yield for NTS and Eurasian (PNE and Novaya Zemlya) events at GIL.

T_d versus Yield

GIL

○ KAZAKH Δ ∿ 59.9 - 60.3°

▲ YUCCA TUFF

T_d (sec)

1.5
1.4
1.3
1.2
1.1
1.0
0.9
0.8
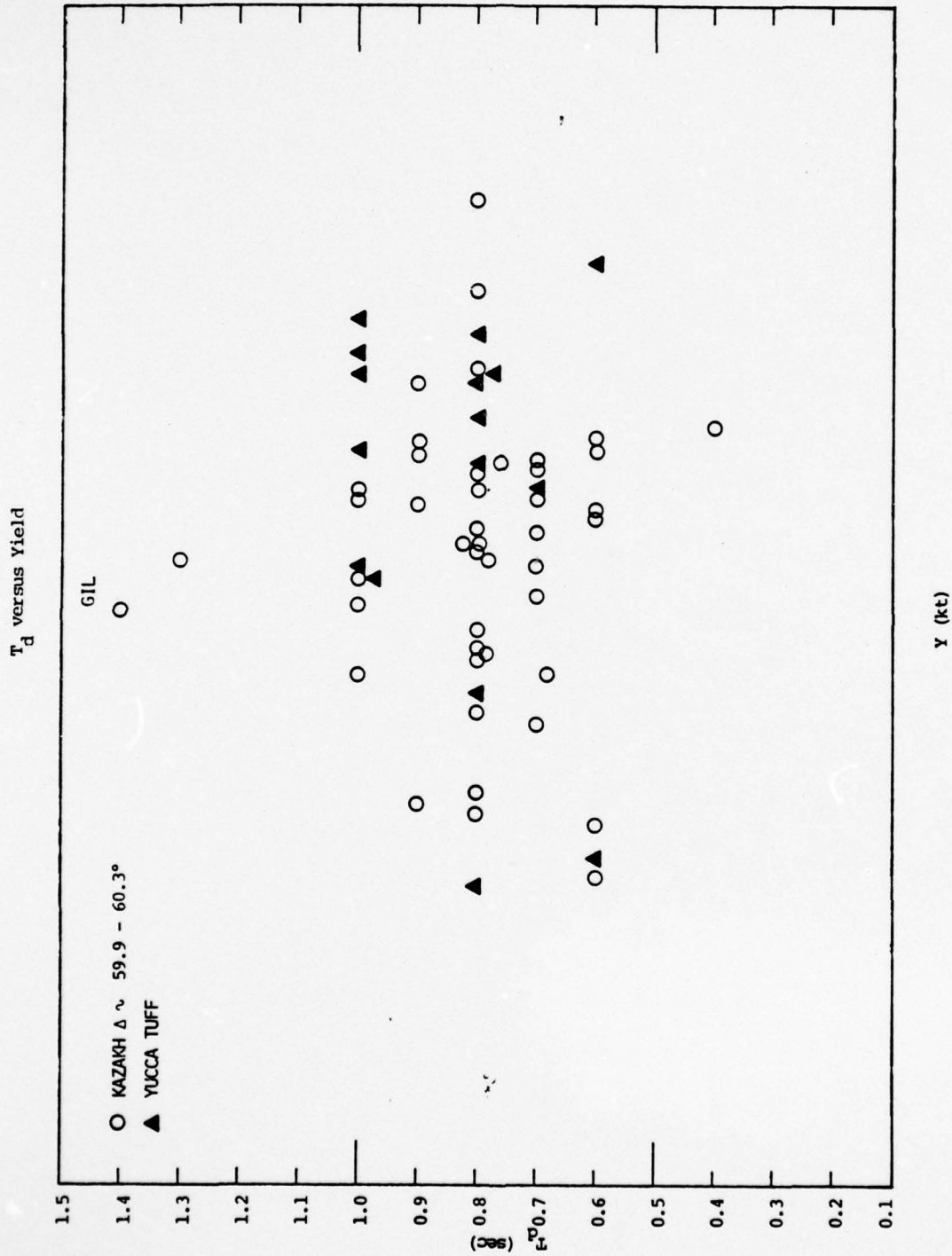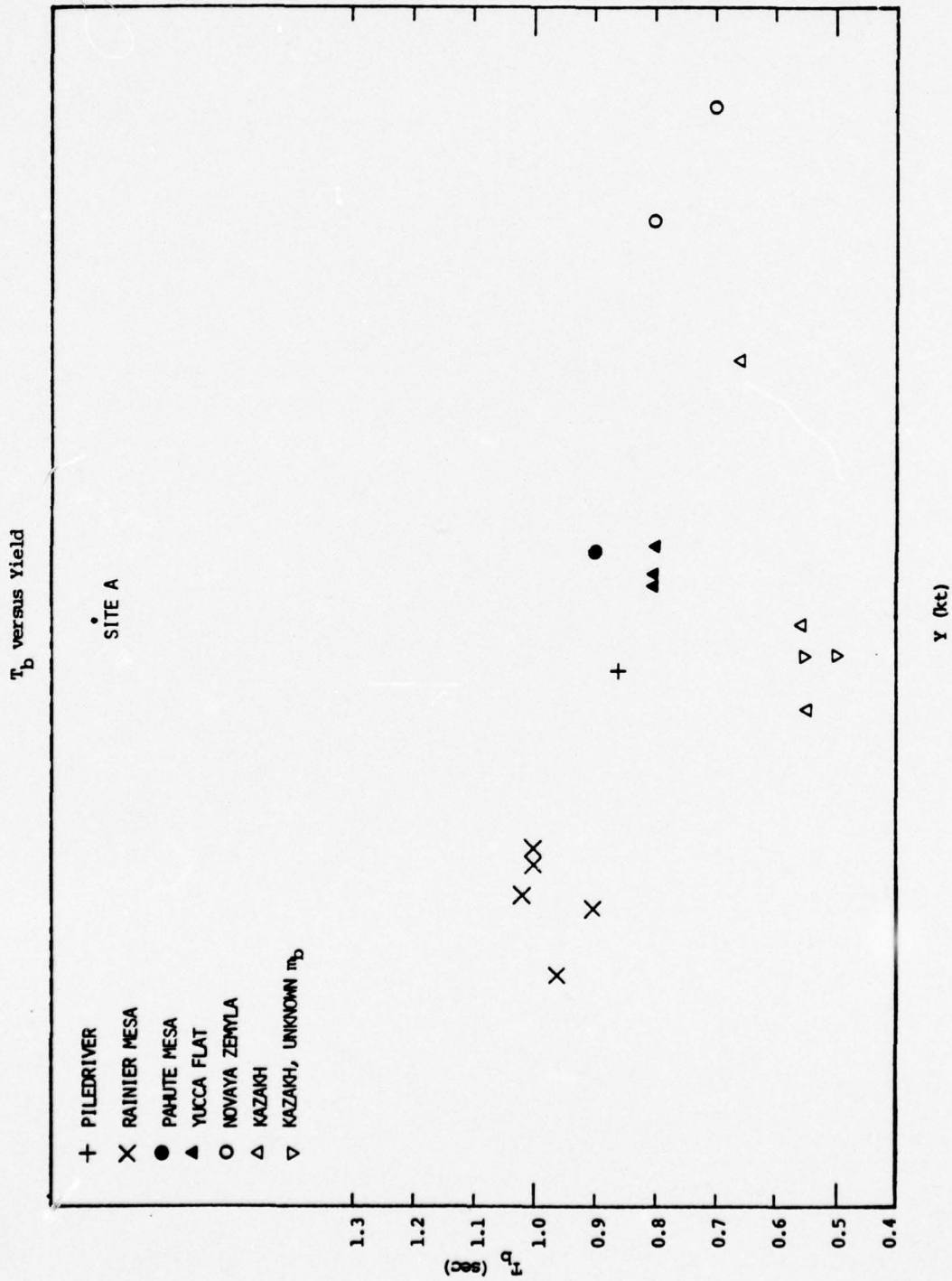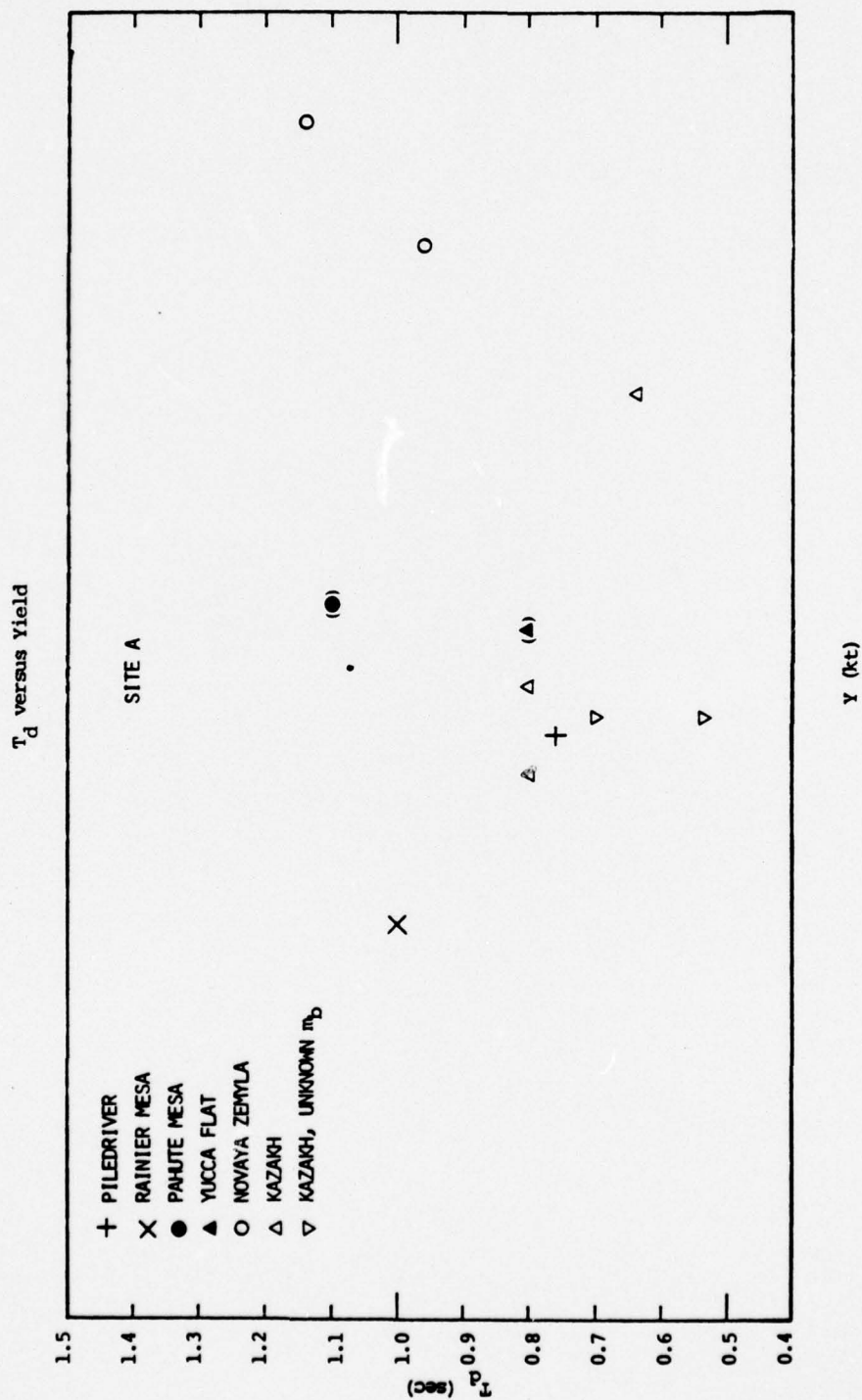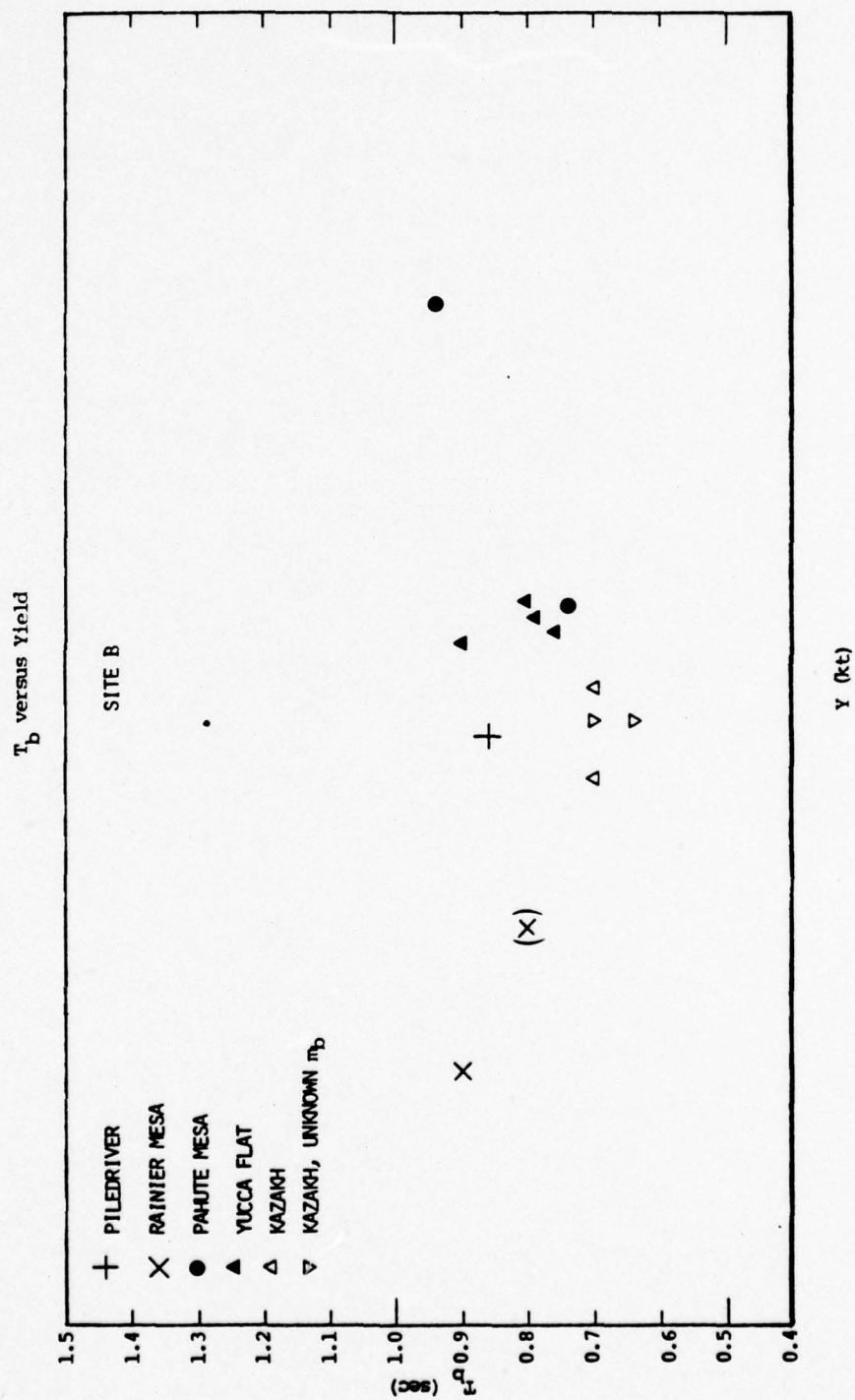0.7
0.6
0.5
0.4
0.3
0.2
0.1

Y (kt)

Figure 3.2.12. T_d versus yield for NTS (Yucca) and east Kazakhstan events at GIL.

Figure 3.2.13. T_b versus yield for explosions recorded at SITE A.

50

Figure 3.2.14. T_d versus yield for explosions recorded at SITE A.

Figure 3.2.15. T_b versus yield for explosions recorded at SITE B.

3. There is no apparent dependence of dominant period, either T_b or T_d, on event yield for east Kazakhstan explosions.

4. In the case of NTS events, there is no observed dependence of period on yield at the station PMS. At the stations KDC and ADK, however, dominant periods tend to increase with increasing explosion yields.

5. At PMS, the only station of the three in question for which data from Eurasian explosions not located in east Kazakhstan are available, there is an apparent lengthening of dominant period with increasing event yield. An important point to note, however, is that these events occur in different source regions at significantly different epicentral distances from PMS complicating any interpretation.

The observations from the remaining Palmer station, GIL, are included here to point up the problem of relying on data from a single station. In Figures 3.2.10-3.2.12, values of the dominant periods are plotted versus explosion yield for the event populations considered previously. In contrast to the pronounced separation of event populations seen previously, the estimates of T_b and T_d for the Eurasian (east Kazakhstan and PNE's) and NTS explosions overlap significantly. In fact, the mean T_b for east Kazakhstan events is slightly longer (0.85 sec) than that for NTS events (0.75 sec). For PNE versus NTS events, the mean values of T_b are approximately equal. The apparent reversal of T_b for east Kazakhstan, or near equality for the PNE, versus NTS events is attributed to an obvious phasing of the GIL seismograms of Eurasian events. This phasing (later arrival) results in longer apparent periods when the measurements are made according to the convention described in Figure 3.2.1.

53

The final set of figures shown here (Figures 3.2.13-3.2.15) compare dominant periods for several Eurasian events with a few NTS explosions including, in particular, the PILEDRIVER event. These data were obtained from two AEDS stations at teleseismic distances from NTS. Data from PILEDRIVER were not available from the Palmer stations since the Palmer network began operating during September 1967, more than one year after the occurrence of PILEDRIVER.

As in the case of the Palmer stations PMS, KDC and ADK, the estimates of T_b for NTS events, including PILEDRIVER, are longer than T_b estimates for Eurasian explosions in the same yield range. A significant point about the PILEDRIVER explosion is the fact that it was detonated in granite and was characterized by a fairly short pP-P lag time compared to other NTS events of comparable yield. It is clear from the results in Figures 3.2.13-3.2.15, however, that this apparently does not influence the observed T_b estimates relative to the other NTS events.

3.2.4 Conclusions

As noted at the beginning of this section of the report, the frequency content of explosion P waves recorded at teleseismic distances is primarily controlled by the explosion source function, pP-P lag time and the anelastic properties of the source-to-receiver propagation path. Our observations indicate that P waves from Eurasian events, particularly those originating at east Kazakhstan, are of significantly higher frequency than P waves from NTS events recorded at the same stations. While these data do not argue conclusively for differences in attenuation beneath the NTS and Eurasian test sites being the cause of the observed period (frequency) differences, this is the suggested explanation in view of the large sampling of different event depths (pP-P lag times) and source media.

The data described here provide important constraints on our waveform predictions for Eurasian events. Given independent estimates of pP-P lag times (i.e., based on spectral nulls) and a range of predicted source functions, we will be able to estimate values of t* for the different test site-to-receiver paths by matching the observed frequency content of seismograms.

3.3 DEVELOPMENT OF IMPROVED TECHNIQUES FOR ONE-DIMENSIONAL NUMERICAL SIMULATION OF EXPLOSIONS

3.3.1 Introduction

During the past several years we have been developing constitutive models and stress wave propagation techniques for modeling underground nuclear explosions [e.g., Cherry, et al., 1973; 1975]. The computational techniques developed are capable of simulating the explosion induced shock wave from the near source high pressure regime out into the region where the material response is linearly elastic. Most of our calculations have been carried out in a one-dimensional (spherically symmetric) geometry for which we use the computer program we call SKIPPER.

In recent months we have needed to compute the equivalent elastic source for explosions in highly porous materials exemplified by the dry tuffs occurring at shallow depths at Yucca Flat, NTS. Our procedure for computing the equivalent elastic source is to monitor the displacement field in the linear elastic field and, using quasi-analytic techniques, to obtain a reduced displacement potential (RDP) representation of the field. In essence we invert the differential equation

$$u(t-R/\alpha) = \frac{\Psi(t-R/\alpha)}{R^2} + \frac{\dot{\Psi}(t-R/\alpha)}{R\alpha} , \qquad (3.3.1)$$

to obtain the RDP, Ψ.

A satisfactory RDP must exhibit the following characteristics [Cherry, et al., 1973]:

1. The RDP should be invariant with distance, R.

2. When $\dot{u} = 0$, we should have $\dot{\Psi} = 0$.

3. At long time the Ψ is constant ($\Psi \rightarrow \Psi_\infty$) and $u_\infty = R^2 \Psi_\infty$.

Typical results for an explosion calculation in tuff with 14.5 percent air-filled voids are shown in Figure 3.3.1. Examining the figure, it is clear that the results violate the three conditions listed above. We point out that for materials with less air-filled porosity, the three conditions are satisfied with considerable accuracy. In fact, this is required to match analytic solutions such as that by Blake [1952], a check carried out at the time SKIPPER was developed [Cherry, et al., 1973].

In view of the failure of SKIPPER to properly handle waves in highly porous materials, the constitutive models were reviewed and tests against analytical results were initiated to circumvent this difficulty. The results of this effort are described in the sequel.

3.3.2 An Improved Constitutive Model for Wave Propagation In Porous Materials

A series of elastic test problems were initiated to test the ability of SKIPPER to propagate elastic waves. Monitoring the pressure versus volume, it was confirmed that loading and unloading occurred on the same path. Further, the numerical results agreed very well with analytical solutions as long as the maximum pressure was small compared to the elastic limit pressure, p_e. However, the differences became noticeable as the maximum pressure increased to a significant fraction of p_e.

The observations stated above suggest that the difficulty is in the fact that while the code is elastic, it is not linear elastic as the p-V relation has significant curvature for pressures near p_e. While this was known, the extent of the effect on the solution was not known.

The problem and its solution are summarized graphically in Figure 3.3.2. In (a) we show the p-V curve in its original form for porous materials. Even though the material
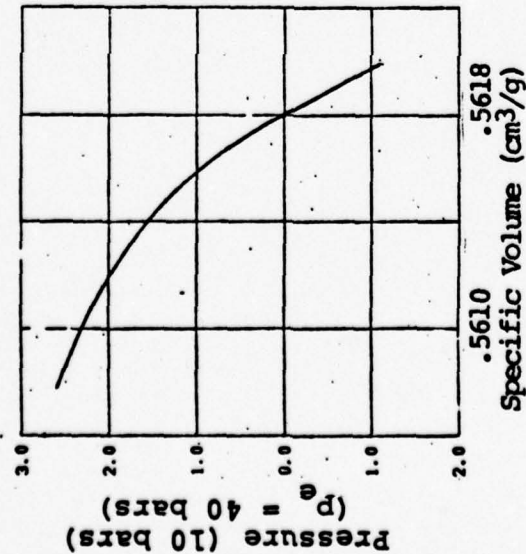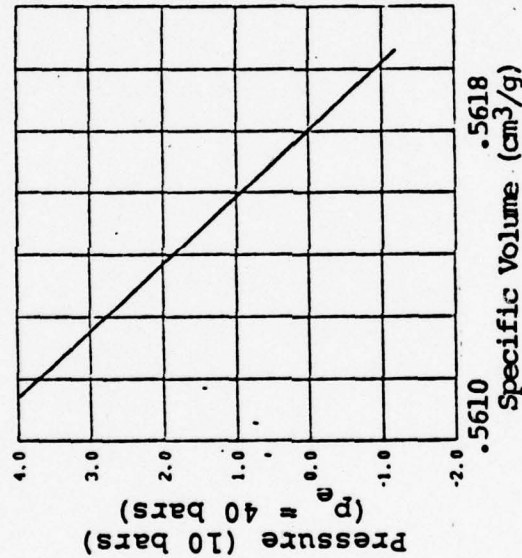
57

a. u, $\dot{u}$, Ψ, $\dot{\Psi}$ at R = 54.7 m
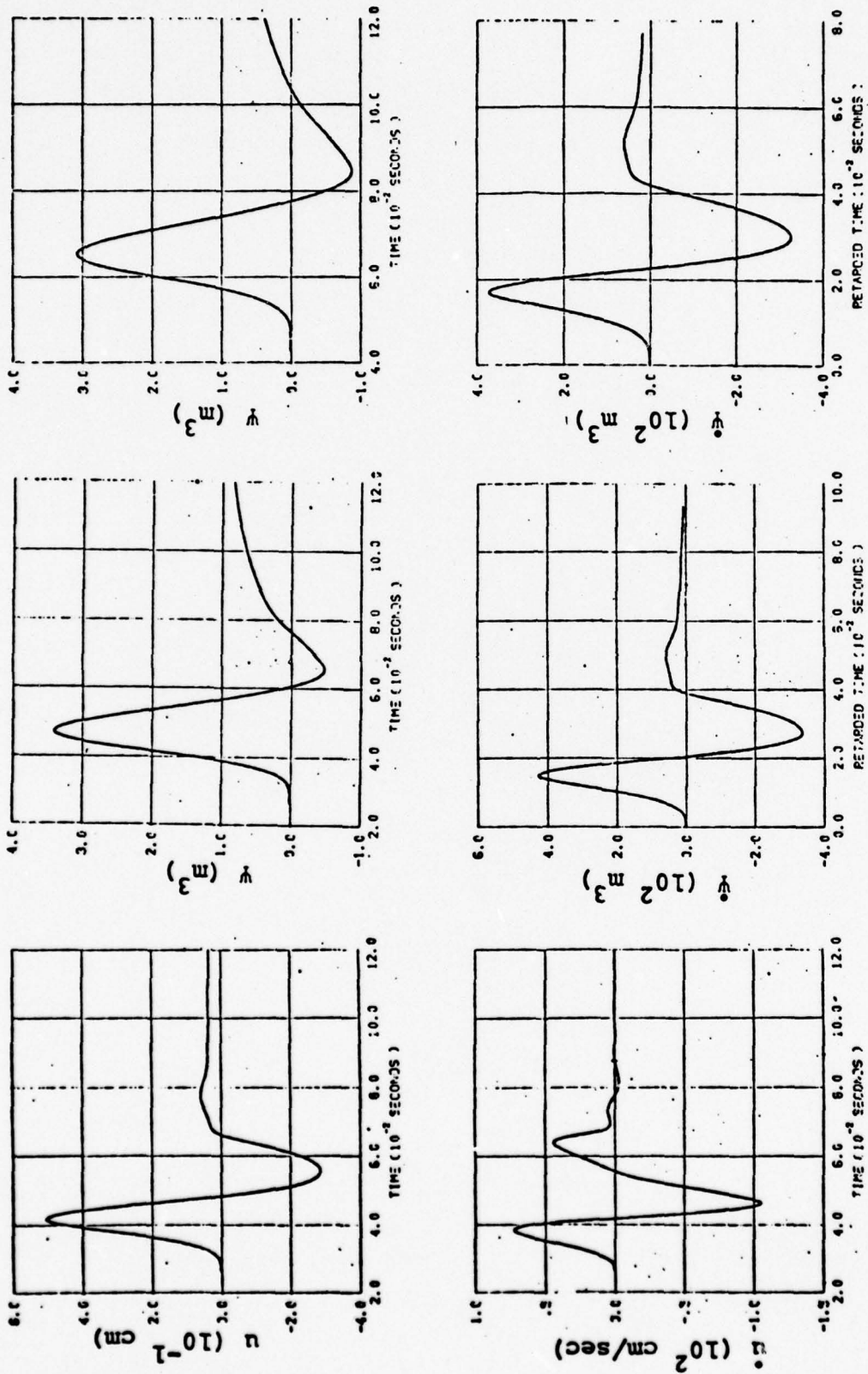
b. Ψ, $\dot{\Psi}$ at R = 87.5 m

Figure 3.3.1. Displacement, velocity and potential time histories for an explosion in dry tuff with 14.5 percent porosity using the constitutive model reported by Cherry, et al., 1975. The calculation is for a yield of 0.02 kt.

c. p-V relationship for porous material calculations in SKIPPER

b. Adjusted p-V curve for elastic test problem

a. Original p-V curve for elastic test problem

Figure 3.3.2. Pressure-volume relationships for porous materials. Note that parts a. and b. show only the elastic portion of the crush curve. Part c. shows the elastic portion and the transition region between the new linearly elastic portion of the crush curve and the unchanged nonelastic region.

59

loads and unloads along this line (elastic behavior), there
is significant deviation from linearity for large changes in
pressure. For our elastic test problems to be compared to
analytic solutions, we merely forced the p-V relation to be
linear as indicated in Figure 3.3.2b. An alternative solu-
tion is to choose a lower pressure as the elastic limit.
Although this method would clearly work, it would increase
the cost of the calculations and probably would not pro-
duce results significantly different from the solution
chosen.

In a full explosion calculation it is necessary to
have a p-V relationship that extends into the nonlinear re-
gime. The adjusted p-V relation for the porous tuff calcula-
tion of Figure 3.3.1 is shown in Figure 3.3.2c. The data
were made linear to p_e and a smooth transition between p_e
and the nonlinear portion of the crust curve was introduced.
This modification in the material behavior does not contra-
dict available laboratory data.

The calculation described in Figure 3.3.1 was repeated
with the minor modification described above. The results
are shown in Figure 3.3.3. We see that now the calculations
satisfy the three conditions of Section 3.3.1 quite well.

Our ultimate objective in computing RDP's for under-
ground explosions is to determine the effect of local material
properties on such gross measures of seismic energy as m_b
and M_s. The question is, how much has our adjustment of the
constitutive model affected these quantities. The answer is
apparent from Figure 3.3.4 where we show the amplitude of the
Fourier transformed reduced velocity potential ($|\hat{\Psi}(\omega)|$) for
the two calculations. The source functions are appropriate
for a yield of 20 kt.

The m_b is controlled by the portion of the spectrum
from $\approx 0.8 - 2.0$ Hz. The M_s is sensitive to the long period
spectrum with frequencies from $\approx 0.04 - 0.1$ seconds. Com-
paring the two source functions we see that in this case

60

a. u, $\dot{u}$, $\ddot{u}$, ψ, $\dot{\psi}$ at R = 23.0 m
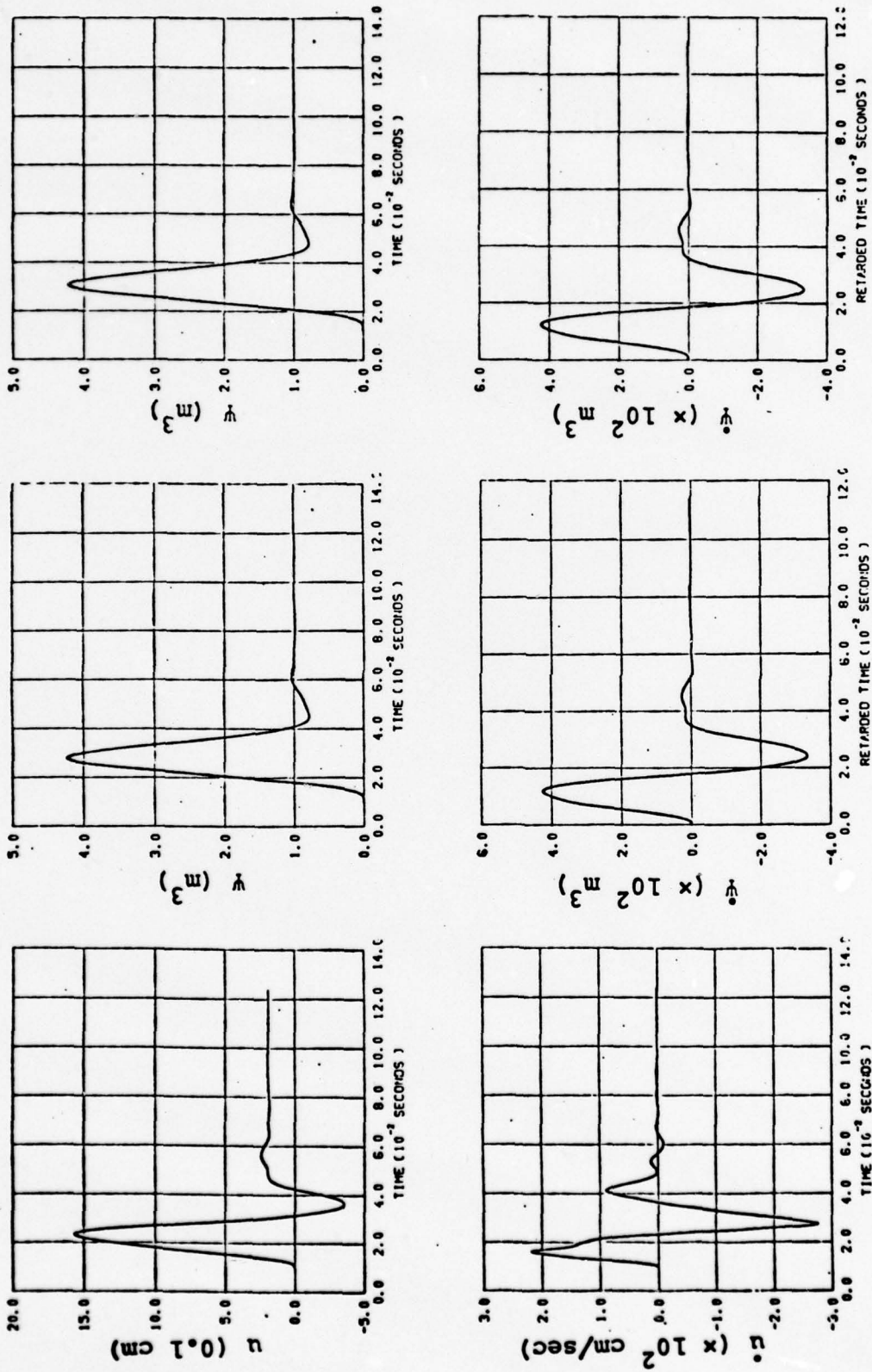
b. ψ, $\dot{\psi}$ at R = 28.0 m

Figure 3.3.3. Displacement, velocity and potential time histories for an explosion in dry tuff identical to that of Figure 3.3.1 except that a linear p–V relation has been introduced below Pe.
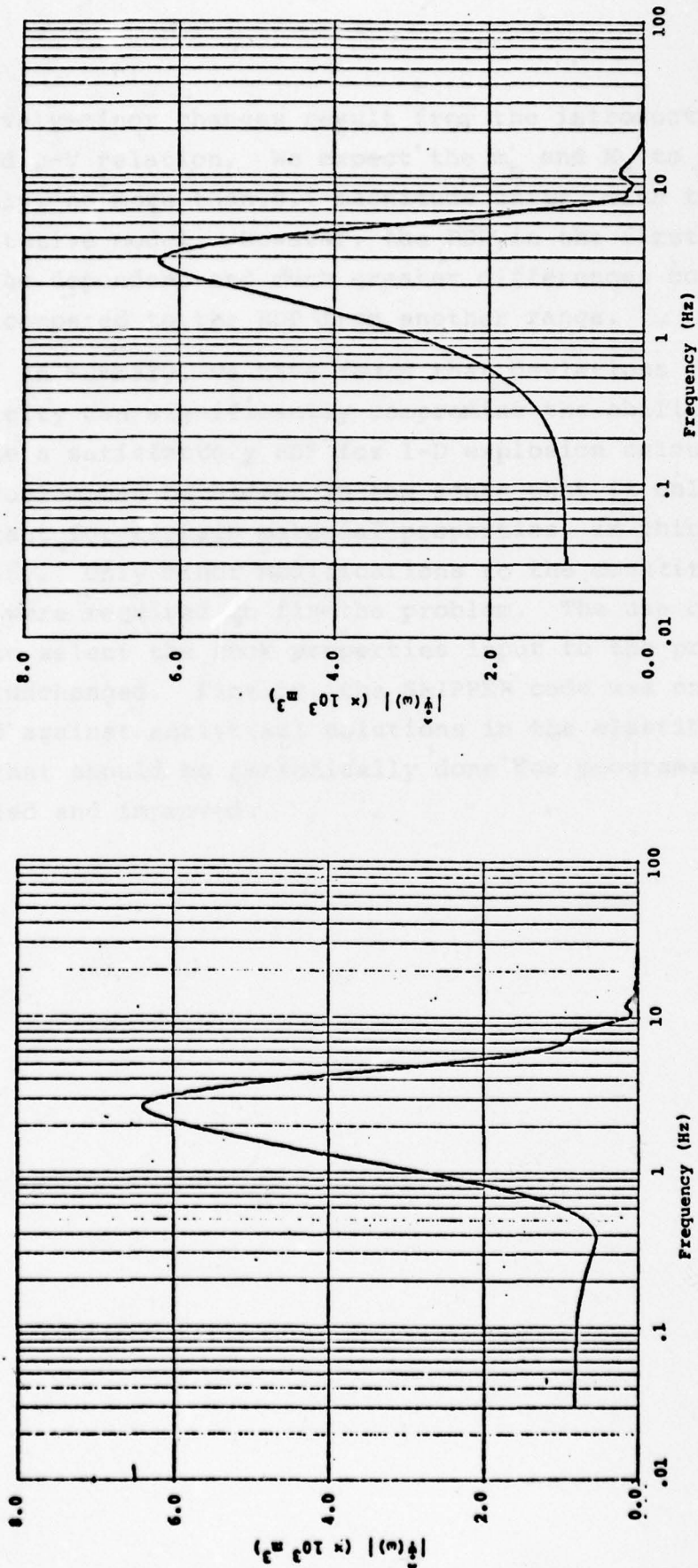
61

Figure 3.3.4. The amplitude of the Fourier transformed reduced velocity potential for a 20 kt explosion in dry tuff with 14.5 percent air-filled porosity. The plot on the left is for the original constitutive model. On the right is the $|\dot{\psi}(\omega)|$ for the modified constitutive model with a linear p-V relation below Pe.

relatively minor changes result from the introduction of the altered p-V relation. We expect the m_b and M_s to increase slightly, no more than 0.1 magnitude units, with the improved constitutive model. However, the RDP in the first calculation is range dependent and much greater differences could result if we compared to the RDP from another range.

In summary, we have found that deviations from linear elasticity can significantly compromise the ability to compute a satisfactory RDP for 1-D explosion calculations. The problem can be hidden in the sense that it only becomes important for certain material properties, in this case high porosity. Only minor modifications to the constitutive model were required to fix the problem. The use of laboratory data to select the rock properties input to the program remains unchanged. Finally, the SKIPPER code was once again tested against analytical solutions in the elastic regime, a test that should be periodically done for programs being modified and improved.

3.4   THE DEPENDENCE OF BODY WAVE MAGNITUDE ON YIELD FOR
       UNDERGROUND EXPLOSIONS IN SALT

A theoretical study was conducted in which the objective was to compare explosions in salt in Eurasia to similar, though hypothetical, events at NTS and to granite events at NTS. The results of this study were reported in detail in a topical report by Bache, Cherry and Mason [1976]. In this report we reproduce the main results from the topical report and give some additional results: theoretical spectra for several of the calculations.

The equivalent elastic source, the reduced displacement potential, was computed for four explosions in salt in which only the overburden pressure was varied. The source spectra are shown in Figure 3.4.1. The relationship between the $\hat{\Psi}(\omega)$ and the far-field displacement spectrum is given by Eq. (3.1.2).

From the spectra of Figure 3.4.1, we see that the long period level is mildly sensitive to depth, varying by only 20 percent over the entire range. However, the short period level varies by a factor of 2.2 from largest to smallest. This is because of the marked peaking of the source function at shallow depths. This peaking is due to the opening of tensile cracks in the material at low confining pressures.

The sources of Figure 3.4.1 were used to compute synthetic short period seismograms at teleseismic distances. A key parameter for these calculations is the attenuation parameter t*. For paths such as NTS-Alaska that we have studied extensively, we believe t* $\approx$ 1.0. Because we believe t* is lower for Eurasian travel paths we rather arbitrarily have chosen t* = 0.6 for these calculations.

The computed synthetic seismograms for a particular range are shown in Figure 3.4.2. The source function, yield and burial depth for each calculation are printed on the
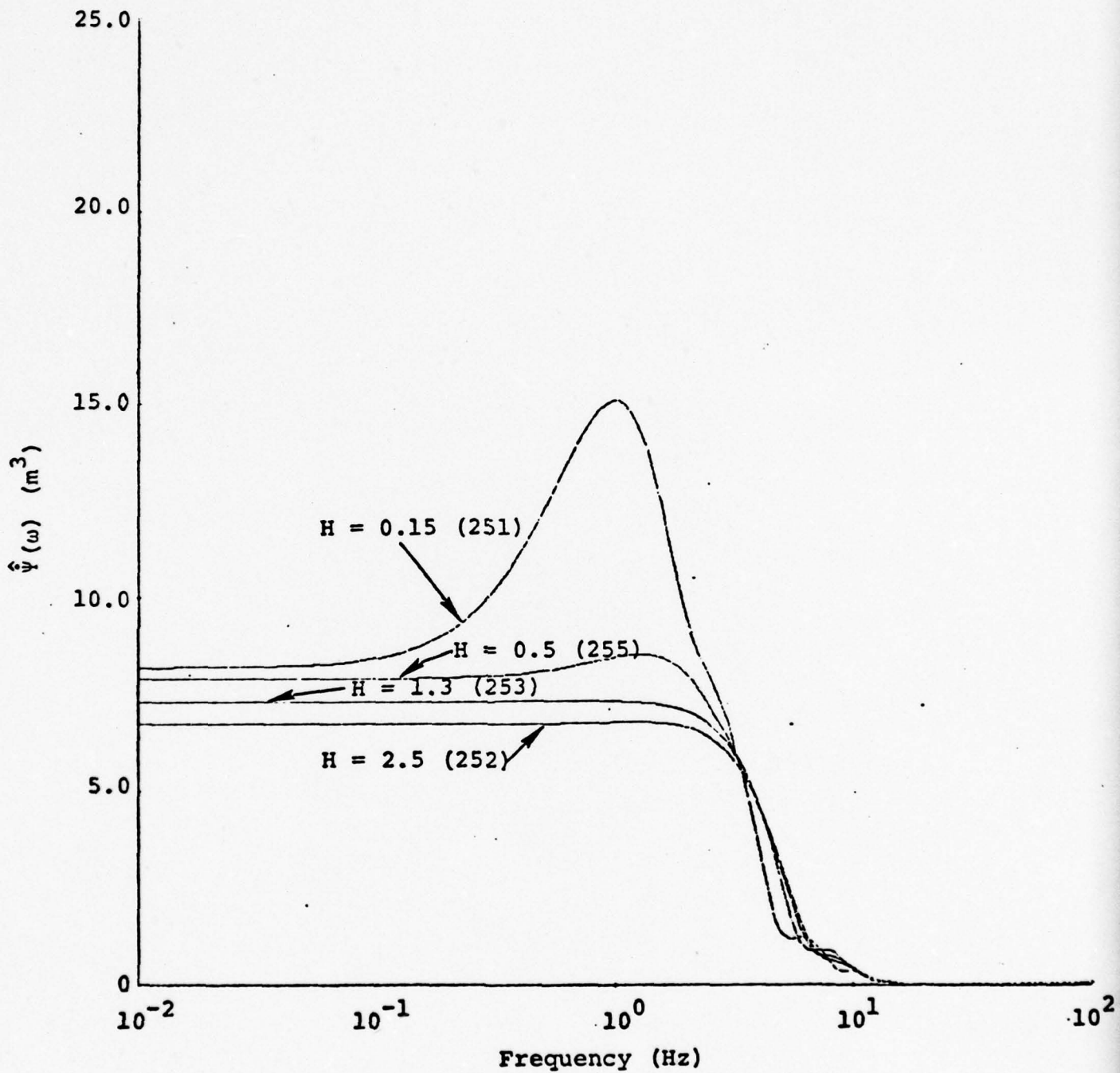
64

Figure 3.4.1. Source functions for salt with variable over-
burden (indicated by the depth H, in km). The
frequency axis is scaled to 160 kt, the ampli-
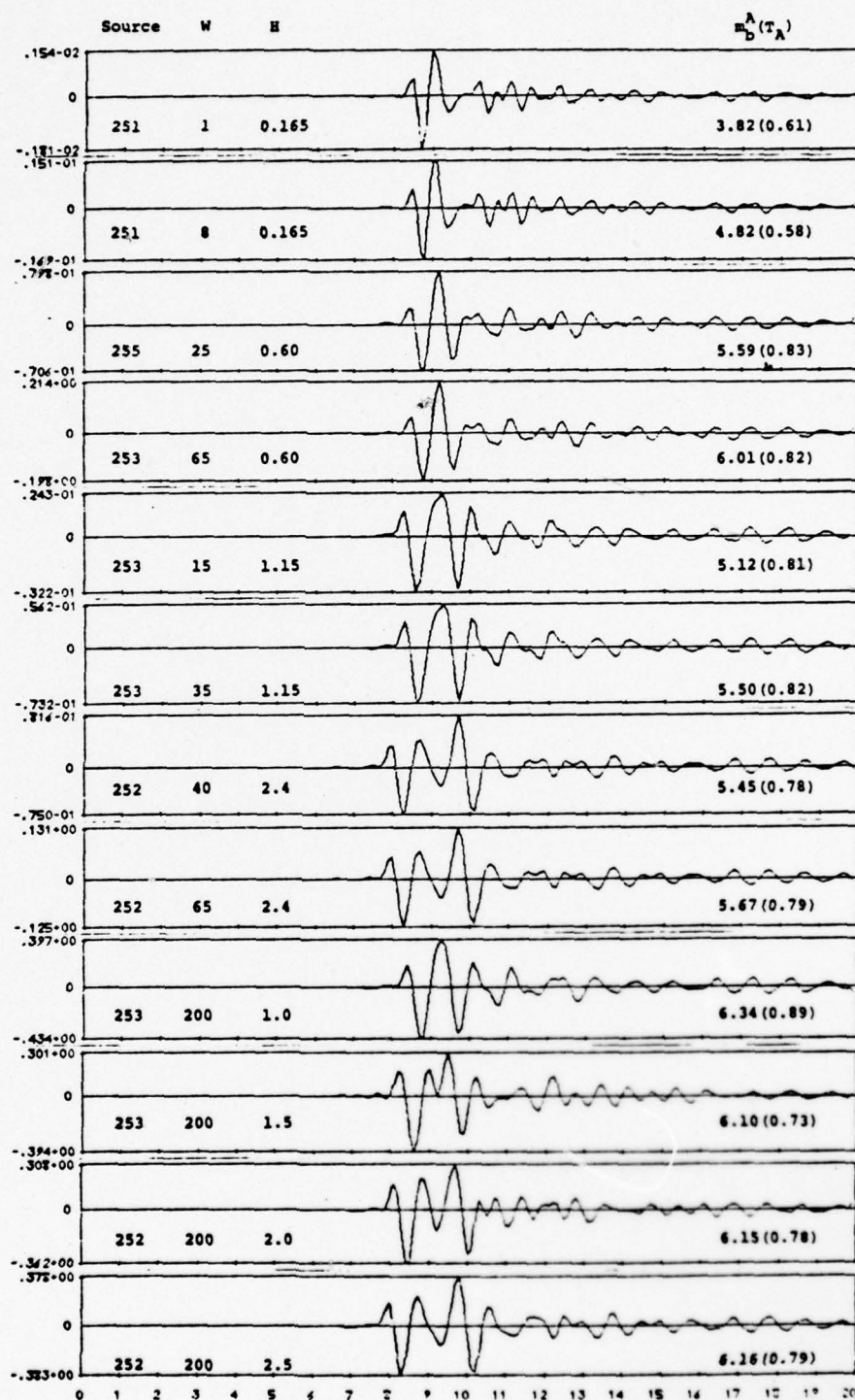tude axis to 0.02 kt.

Figure 3.4.2.   Synthetic seismograms at 56.6°.   The numbers at the left are ground motion in microns at 1 Hz.

records. Also appearing on the records are the m_b values and the period of the cycle at which m_b is measured.

In Figure 3.4.3 we plot m_b versus log yield (W) from the synthetic seismograms. The best least squares linear fit to the data was computed for the total group and two sub-groups depending on the scaled depth of burial.

We next change the path parameters to be appropriate to the NTS-Alaska travel path that we have previously calibrated. The most important change is now t* = 1.06. Synthetic seismograms were computed for five of the twelve events of Figure 3.4.2. The seismograms are shown in Figure 3.4.4.

We are also interested in comparing m_b-yield for the salt events to that for explosions in granite. We have previously [Bache, et al., 1975] computed a theoretical m_b for PILEDRIVER that agrees quite well with observations. We expect the m_b-yield curve for NTS granite explosions would be close to a curve of unit slope through the PILEDRIVER datum.

The m_b-yield values for salt-Eurasian travel path, salt-NTS travel path and PILDRIVER granite-NTS travel path are compared in Figure 3.4.5. Three lines of unit slope are shown through the data. The uppermost line is the least squares fit to the salt-Eurasian path events of Figure 3.1.2. The lowest line is 0.55 magnitude units below the first. This is representative of the difference between the salt-Eurasian path and salt-NTS path m_b values if the t* change from 0.6 to 1.06 is approximately correct.

The unit slope line through the PILEDRIVER theoretical m_b falls almost equidistant between the lines for the two populations of salt events. That is, events like PILEDRIVER are expected to give m_b values that are, on the average, 0.1 - 0.3 magnitude units above those for similar NTS events in salt. On the other hand, the granite events give m_b values that are about 0.1 - 0.3 units lower than Eurasian salt events.
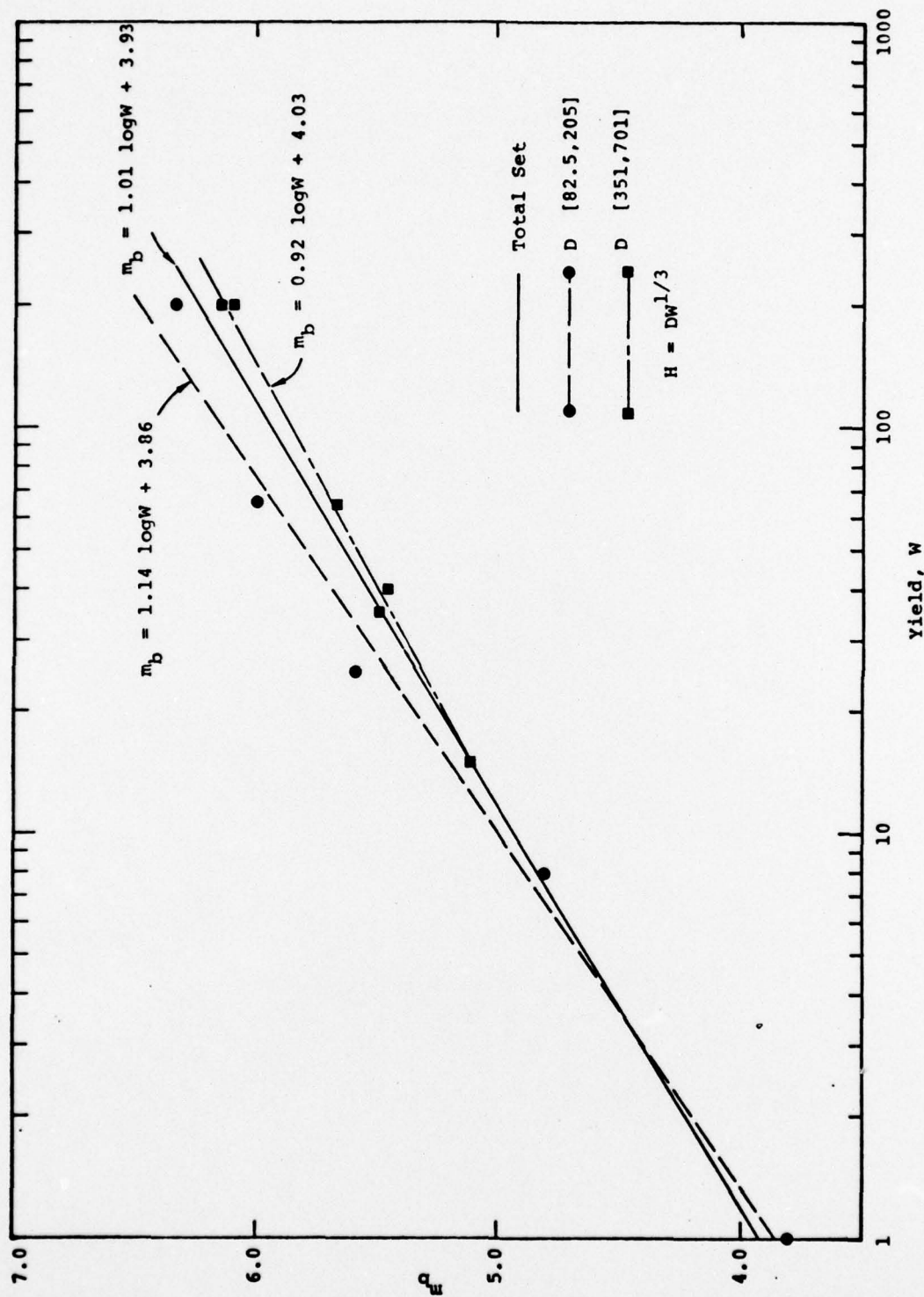
Figure 3.4.3. m_b versus yield at 56.6°. Least square lines are fit to the total data set and to two subgroups divided by scaled depth of burial.
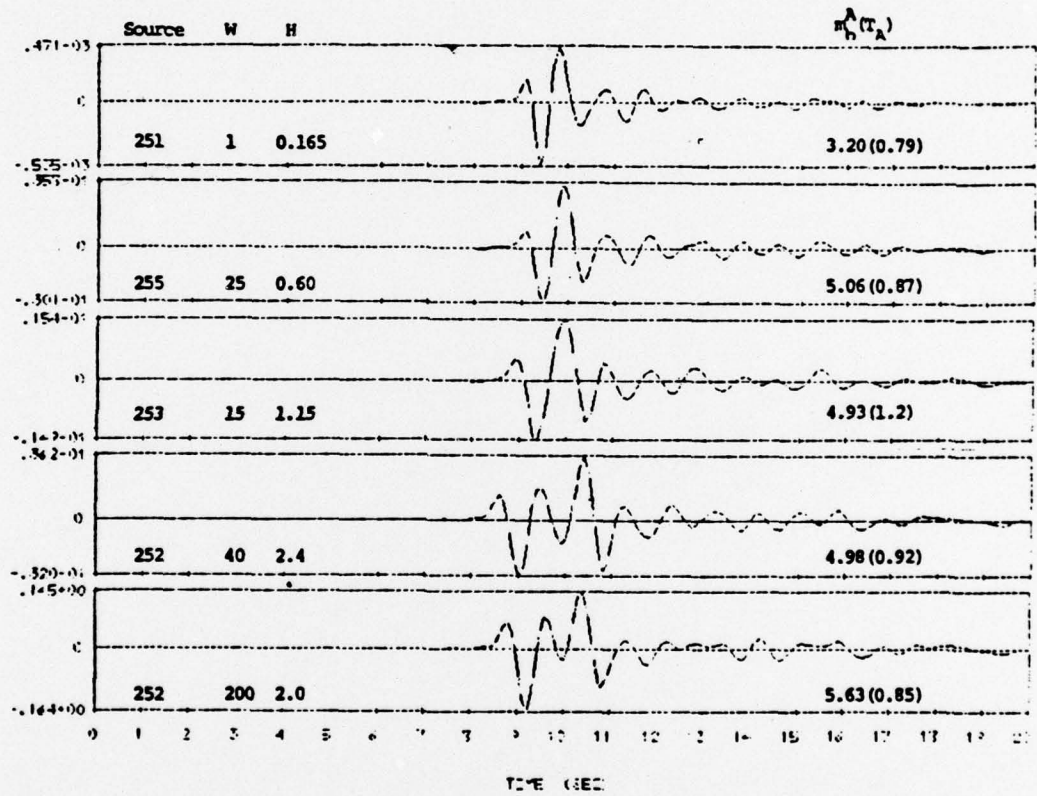
Figure 3.4.4. Theoretical seismograms for hypothetical events in salt at NTS. The source parameters are the same as for the corresponding Eurasian salt events studied in previous sections. The path parameters are appropriate for an NTS-Alaska path.
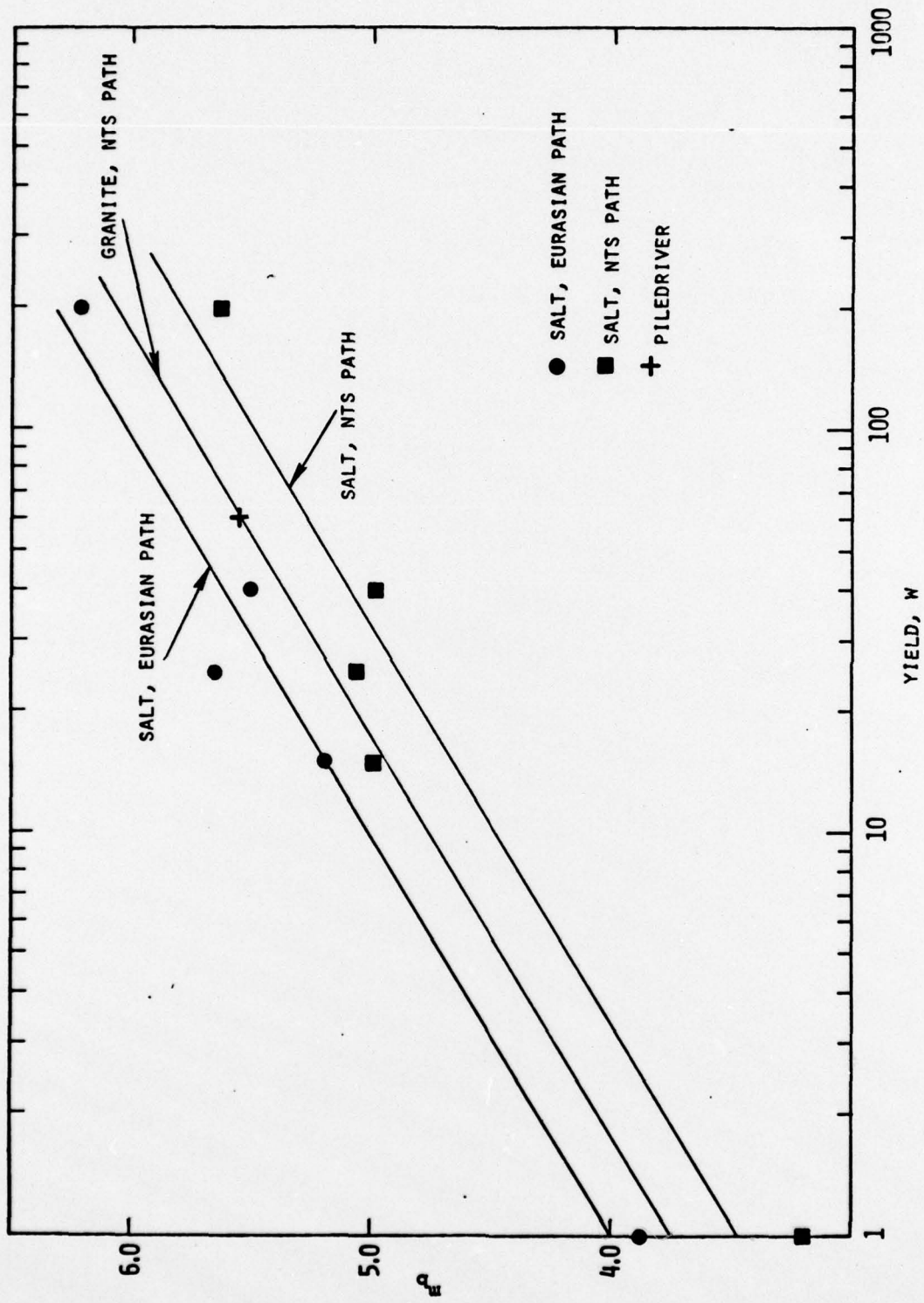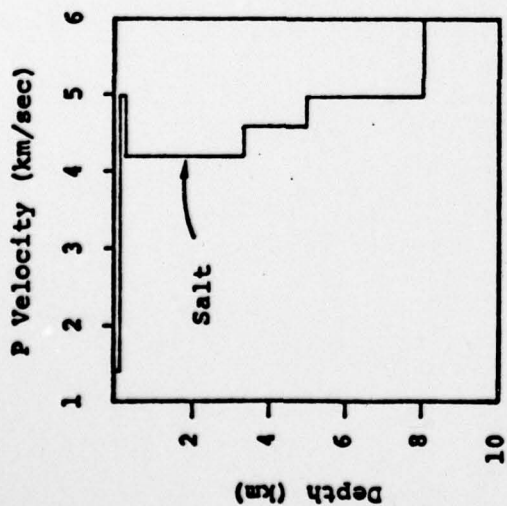
69

Figure 3.4.5.   Comparison of m_b-yield for salt events in Eurasia and at NTS to granite explosions at NTS.
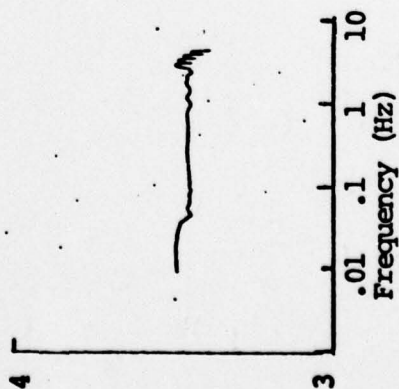
Not presented in the Bache, Cherry and Mason [1976] topical report but of some interest are typical displacement spectra for our theoretical salt events. We select four of the events for which seismograms were presented in Figure 3.4.2. Displacement spectra for these calculations are shown in Figures 3.4.6 - 3.4.7. In Figure 3.4.6a we show the P wave velocity-depth model used for the crust in the source region. The spectra in the figure are for the wave as it exits the bottom of the crust at the source. The highest frequency for the spectral computations was 5 Hz.

The most important feature controlling the shape of the spectra in Figure 3.4.6 is the free surface reflection or pP phase. This point is illustrated in Figure 3.4.5b by the spectrum for one of the events with the crustal model modified to allow the salt layer to extend upwards to infinity. Then the only energy in the spectrum is that which leaves the source downward.

In Figure 3.4.7 we show the spectra at the receiver, with and without the instrument, for the same four events. Once again given for comparison are the spectra for the 40 kt event with the layering above the source removed. For these spectral calculations the Nyquist frequency is at about 0.1 Hz and the portion of the plot below this frequency should be ignored. Note that the spectral modulation due to pP is very much obscured by the other reverberations that shape the spectrum.

71

Figure 3.4.6. Displacement spectra at the base of the crust below the source for four of the salt events for which seismograms are given in Figure 3.4.2.

a. Velocity-depth profile

b. Spectrum with no contribution from waves reflected from above the source
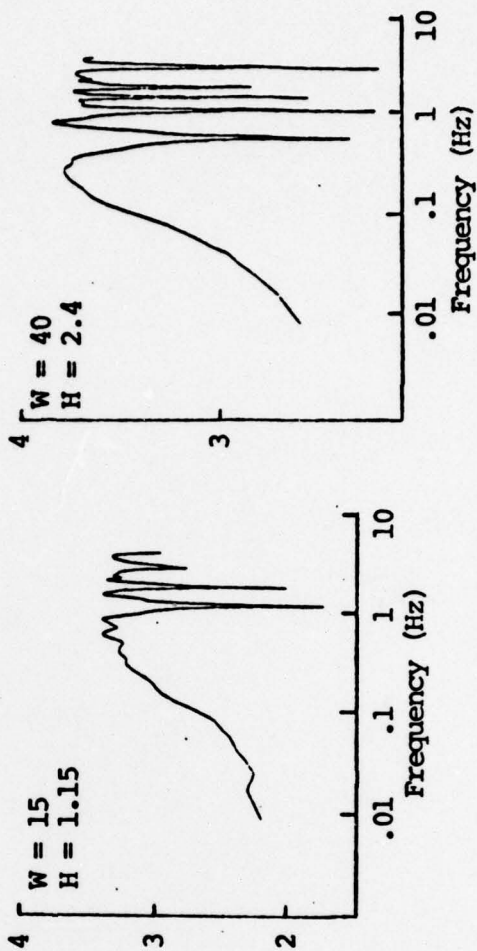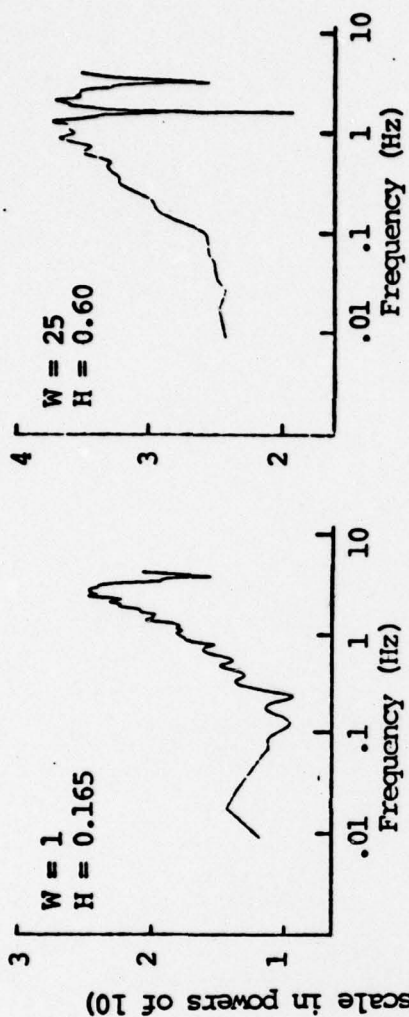
c. Spectra for four events

72

a. Spectra with no contribution from waves reflected from above the source

b. Spectra of seismogram

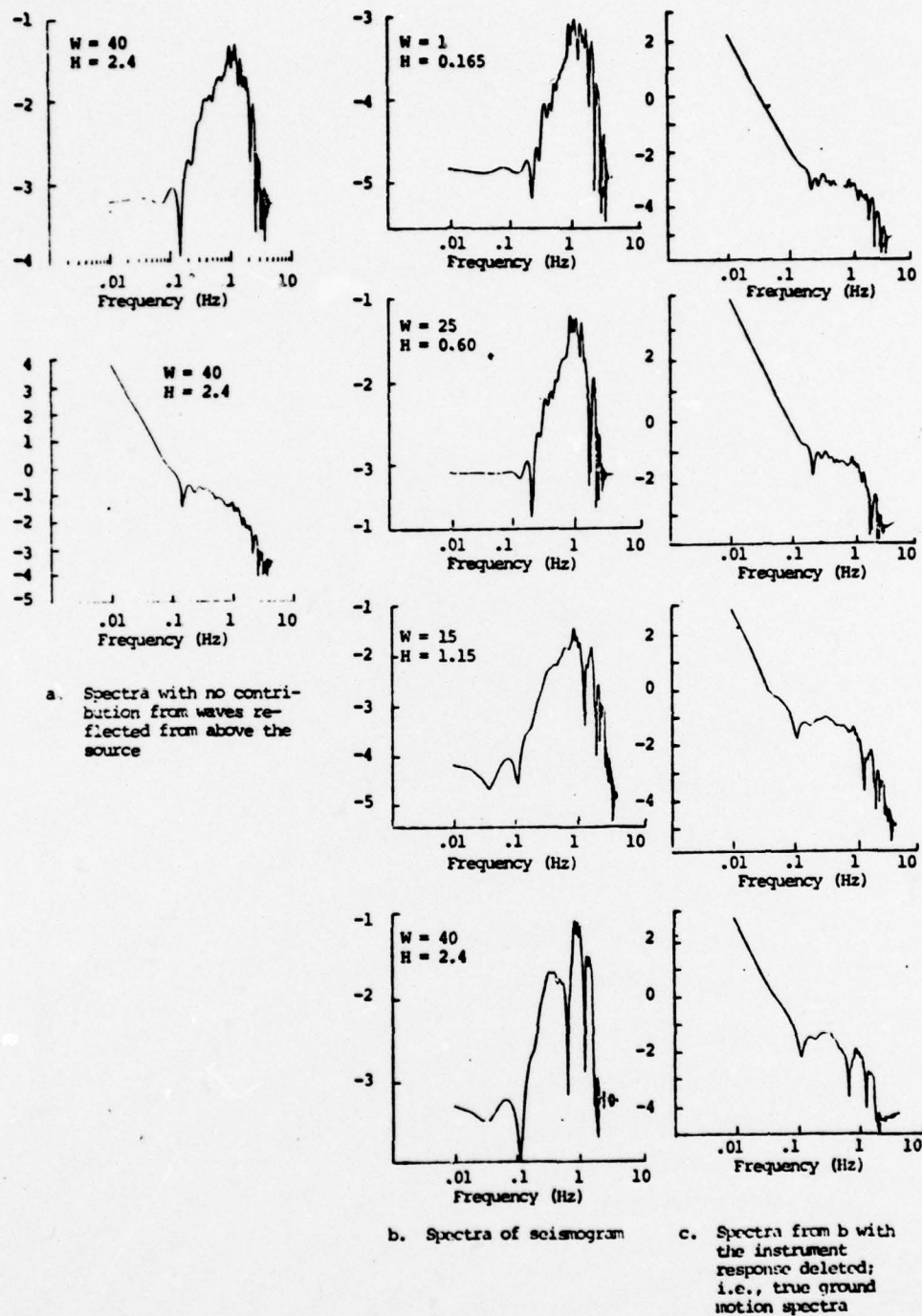c. Spectra from b with the instrument response deleted; i.e., true ground motion spectra

Figure 3.4.7. Ground motion displacement spectra for the events of Figure 3.4.6 with and without the instrument response included.

73

3.5 A LABORATORY SIMULATION OF UNDERGROUND EXPLOSIONS

Carried over from our previous contract (Project VT/ 6712) is a program in which small-scale modeling experiments of underground explosions are being carried out and the results compared to computer simulations of the experiments. During the past quarter, several successful model experiments have been conducted and some results are presented here.

The objective of the experiments is to obtain displacement time histories on the free surface of a uniform medium of well-known properties. The measurements are made on the free surface at large enough distances to ensure that the response is linear elastic.

The test medium was a "high-early" concrete of density 2.52 g/cm^3, unconfined compressive strength 3.45×10^7 Pa (345 bar), low porosity and high water saturation. The observed sound speed was 3.4×10^5 cm/s. Each explosive charge[*] consisted of 1/4 g of PETN, packed to a density of 1.0 g/cm^3 inside a lucite shell of radius 0.56 cm. Great care was exercised in the construction of each charge to ensure that the resulting detonation was spherically symmetric.

The principal sensors were eddy-current displacement gauges.[**] Each unit's output varies linearly with distance between the probe's tip and a small piece of aluminum foil fixed with epoxy to the concrete surface. These transducers have rather low output levels, 2 mV/μm, but they have the advantages that they do not touch the concrete and their response extends to 50 kHz (3 db). To supplement the displacement gauges, we also used two accelerometers[†] with ranges of ± 50,000 g's (5×10^5 m/s^2), sensitivities of 10 μV/g and

---

[*] Supplied by Stanford Research Institute, Menlo Park, CA.
[**] Supplied by Kaman Sciences, Colorado Springs, Colorado.
[†] Supplied by Endevco, San Juan Capistrano, CA.

resonant frequencies above 150 kHz. The low mass of the accelerometers allowed them to be epoxied to the concrete directly.

We prepare the concrete in the form of right circular cylinders of diameter 120 cm and thickness 60 cm. The motion transducers were arrayed over one end of the cylinders and the charges were located 31 cm below those surfaces.

In one experiment, two displacement gauges and an accelerometer were in close proximity and directly over the charge. Our objective was to see if the three independent transducers would give similar responses to the seismic motion. In fact, the responses were quite similar, showing an arrival time of 92 μs, risetime (in displacement) of 15 μs, peak motion of 5 μm and full width at half maximum of about 20 μs.

For the subsequent tests, the gauges were located at the vertices of a one foot equilateral triangle: horizontal (toward vertex #2) and vertical displacement at vertex #1; vertical displacement and acceleration at vertex #2; and vertical acceleration at vertex #3. Charges were placed 31 cm below each vertex and fired one at a time. Some typical results are shown in Figures 3.5.1 and 3.5.2.* While there are several reasons to believe that the double integral of an accleration signal is not equal to the true displacement, especially at late times, the acceleration data do generally confirm the shape and amplitude of the main displacement peak.

As might be expected, Figure 3.5.1 shows that no horizontal motion (H1) occurs until the arrival of the more slowly moving shear wave at about 160 μs. All of the data records also indicate that after the main displacement peak, the surface continues to have a small but consistently positive

---

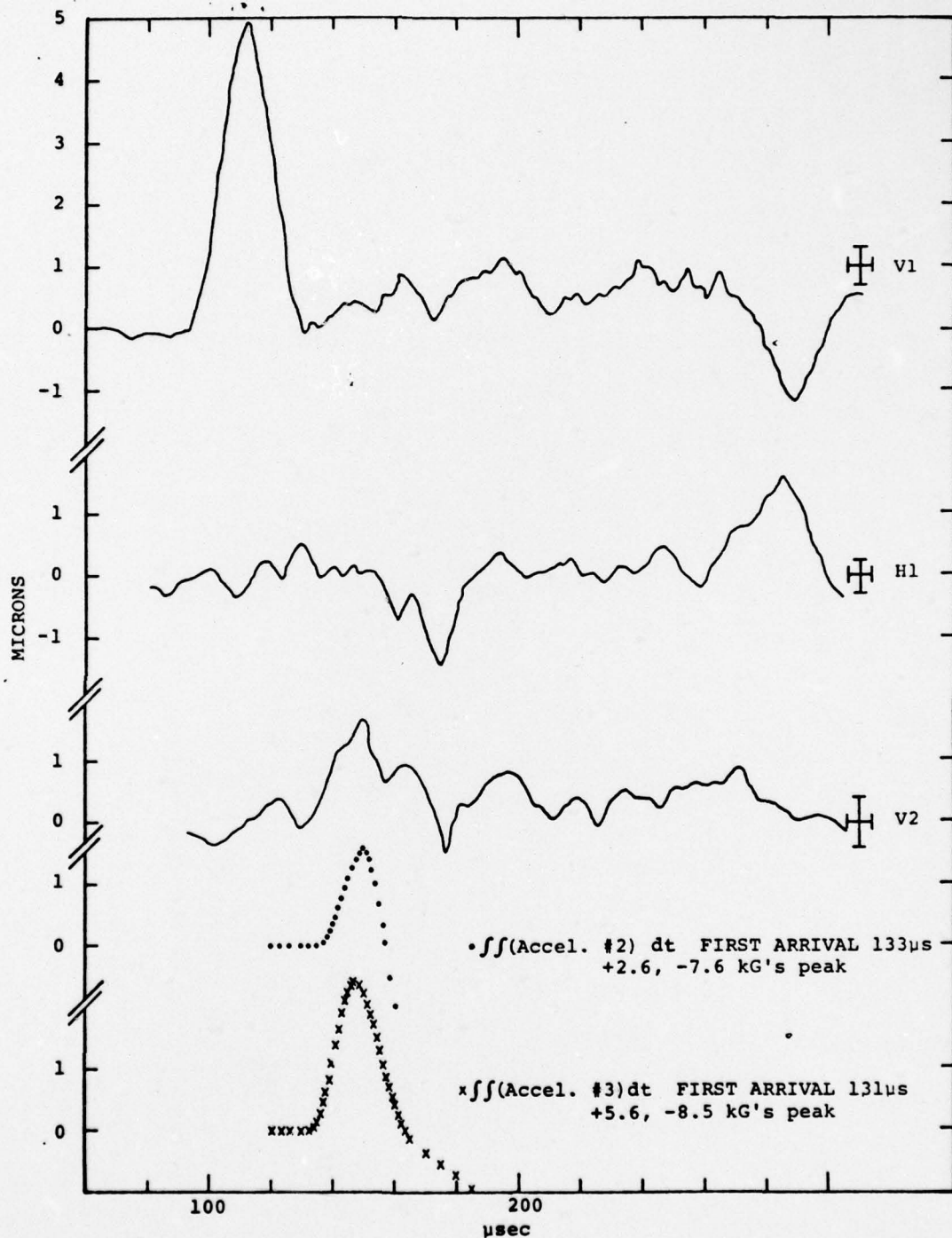*The error bars shown include the uncertainties due to instrument and recorder calibrations and electrical noise.

Figure 3.5.1. Displacement data for the charge emplaced under vertex 1. The vertical and horizontal displacement records at vertex 1 and the vertical displacement record at vertex 2 are shown. Also plotted are the doubly integrated accelerometer records from vertices 2 and 3. For the accelerometer records the time of first arrival and first peak and trough accelerations are indicated.
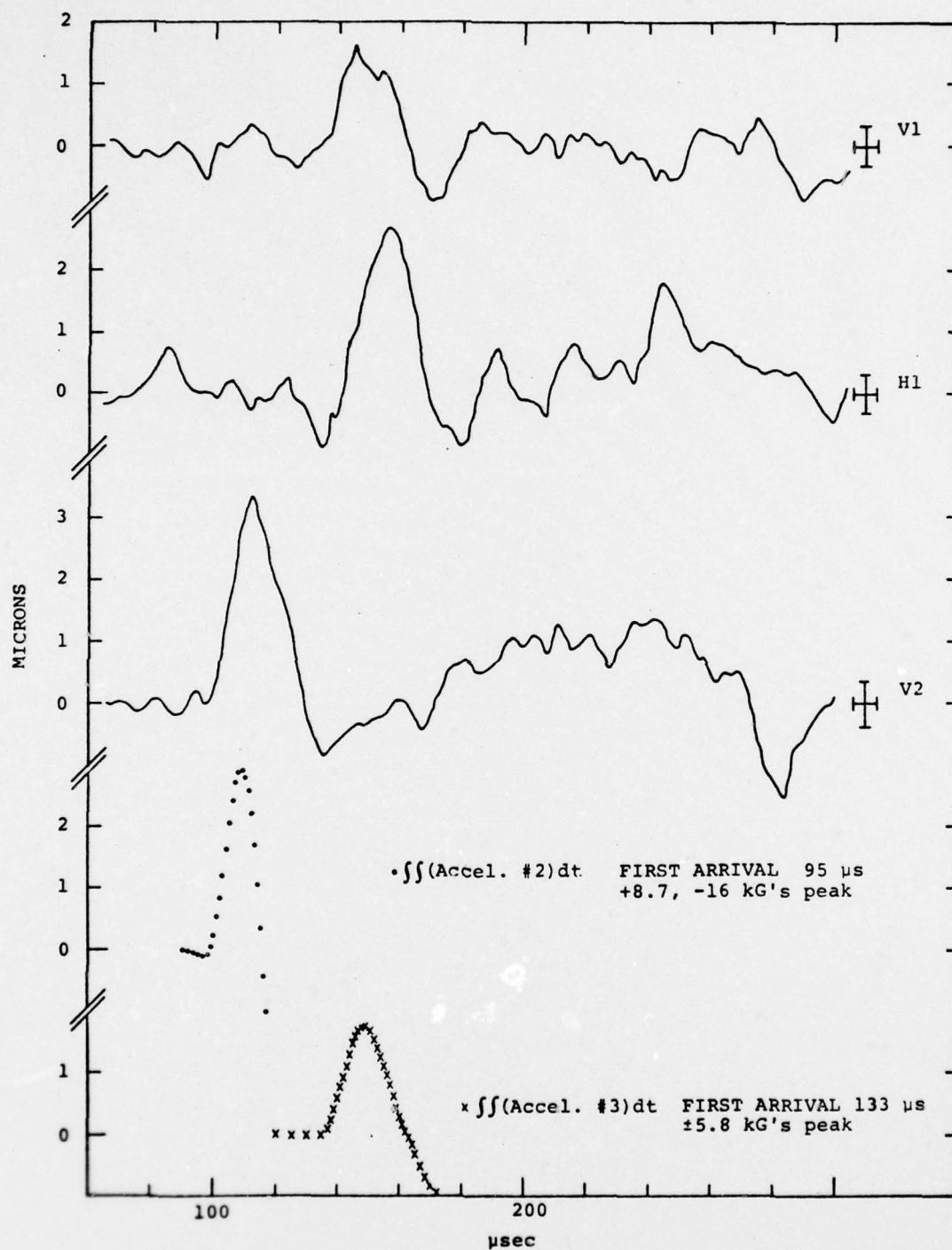
Figure 3.5.2. Data like that in the previous figure except that now the charge is located under vertex 2.

displacement over an interval of at least 100 μs; see V1 in Figure 3.5.1 and V2 in Figure 3.5.2.

The experiments described above will be modeled with our finite difference programs and will thus provide an excellent normalization of the theoretical techniques. Further experiments are also being performed in which the charge emplacement will be shallow and cratering will result.

IV.   REFERENCES

Alewine, R. W., R. W. Klepinger and D. L. Springer, (1975), "Teleseismic P-Wave Magnitude-Yield Relations for Well-Coupled Nevada Test Site Explosions," Unpublished Report.

Bache, T. C., J. T. Cherry, N. Rimer, J. M. Savino, T. R. Blake, T. G. Barker and D. G. Lambert (1975), "An Explanation of the Relative Amplitudes Generated by Explosions in Different Test Areas at NTS," Systems, Science and Software Final Report submitted to Defense Nuclear Agency, DNA3958F, October.

Bache, T. C., J. T. Cherry and B. F. Mason, (1976), "The Dependence of Body Wave Magnitude on Yield for Underground Explosions in Salt," Systems, Science and Software Technical Report, AFTAC/VSC, SSS-R-77-3057 (Draft), November.

Bache, T. C., J. T. Cherry, D. G. Lambert, J. F. Masso and J. M. Savino, (1976), "A Deterministic Methodology for Discriminating Between Earthquakes and Underground Nuclear Explosions," Systems, Science and Software Final Contract Report, ARPA, SSS-R-76-2925, July.

Bache, T. C. and D. G. Harkrider (1976), "The Body Waves Due to a General Seismic Source in a Layered Earth Model: 1. Formulation of the Theory," BSSA, <u>66</u>, pp. 1805-1819.

Blake, F. G., Jr., (1952), "Spherical Wave Propagation in Solid Media," <u>The Journal of the Acoustical Society of America</u>, Vol. 24, No. 2, March.

Cherry, J. T., C. B. Archambeau, G. A. Frazier, A. J. Good, K. G. Hamilton and D. J. Harkrider, (1973), "The Teleseismic Radiation Field from Explosions: Dependence of Seismic Amplitudes upon Properties of Materials in the Source Region," Systems, Science and Software Final Report, DNA 3113Z.

Cherry, J. T., N. Rimer and W. O. Wray, (1975), "Seismic Coupling from a Nuclear Explosion: The Dependence of the Reduced Displacement Potential on the Nonlinear Behavior of the Near Source Rock Environment," Systems, Science and Software Technical Report, AFTAC/VSC, SSS-R-76-2742, September.

Harkrider, D. G., (1964), "Surface Waves in Multilayered Media. I. Rayleigh and Love Waves from Sources in a Multilayered Half-Space," BSSA, <u>54</u>, pp. 627-679.

Harkrider, D. G. and C. B. Archambeau, (1977), "Theoretical Rayleigh and Love Waves from an Explosion in a Pre-stressed Source Region," to be submitted for publication.

Klepinger, R. W., (1974), Unpublished report.

Marshall, P. D. and P. W. Basham, (1972), "Discrimination Between Earthquakes and Underground Explosions Employing an Improved M_s Scale," Geophys. J., <u>28</u>, pp. 431-458.

McEvilly, T. V., (1964), "Central U. S. Crust-Upper Mantle Structure from Love and Rayleigh Wave Velocity Inversion," BSSA, <u>54</u>, pp. 1997-2016.

Tryggvason, E., (1965), "Dissipation of Rayleigh Wave Energy," JGR, <u>70</u>, pp. 1449-1455.